Eindhoven University of Technology

MASTER

Probing spin dynamics in recording media and ultrafast antiferromagnetic to ferromagnetic phase transiton

Bergman, B.

Award date:
2004

Link to publication

TU/e

Eindhoven University of Technology
Department of Applied Physics
Group of Physics of Nanostructures

Seagate
We turn on ideas

Seagate Research
Media Group

Probing Spin Dynamics in
Recording Media and Ultrafast
Antiferromagnetic to Ferromagnetic
Phase Transition

Bastiaan Bergman

July 2004

Seagate advisors: dr. Ganping Ju[a]
                     dr. René van de Veerdonk
                     dr. Julius Hohlfeld
                     dr. Dieter Weller
TU/e advisor: prof.dr. Bert Koopmans[b]

Examination Committee:
prof.dr. B. Koopmans, dr.ir. H.J.M. Swagten, dr. J.E.M. Haverkort, prof.dr.ir.
M.C.M. van de Sanden

[a]1251 Waterfront place, Pittsburgh, PA, USA
[b]Den Dolech 1, Eindhoven, The Netherlands

A traineeship is done at Seagate research in Pittsburgh, PA. In this thesis the improvement and use of an optical pump-probe measurement setup for measurement of magnetization dynamics on picosecond timescales is described.

Precession measurements on perpendicular magnetic recording media (PMR) are done in order to obtain the Gilbert damping parameter as function of various external quantities as well as grain exchange coupling. Strong dependencies are found in PMR media as well as ordinary nickel thin films.

Using the same pump-probe setup temperature driven antiferromagnetic to ferromagnetic phase changes in FeRh thin film are studied. Experimental evidence is given for the phase change to occur on ultrafast (picosecond) timescales when driven by a femtosecond optical pulse. Detailed study of the obtained magnetization dynamics revealed the precessional nature of the dynamic process after the first onset of a ferromagnetic phase. Simulations show high qualitative accordance between the proposed magnetization dynamics and the dynamics as observed.
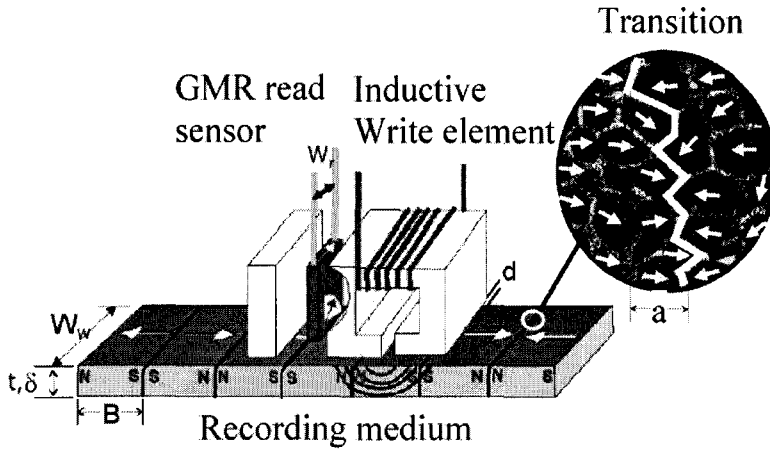
Contents

Figure 1.1: A track in a magnetic recording device such as a harddrive together with a read/write head. Transitions between bits are not straight but follow a zigzag pattern. To reduce noise, broad transitions are necessary to average out the random nature of the grains.

1 Technology Assessment

The general harddrive manufactures' trick has been for decades to double the data-density on a disk and be first on the market. Production costs of a harddrive depend merely on the electromechanical parts and thus on the number of disks in a harddrive. The manufacturer who is first on the market with a harddrive of double storage capacity but for the same production costs doubles his revenue. This powerful mechanism has been pushing the research in magnetic recording for decades and data densities have been doubled every 18 months [1].

Nowadays areal densities reach 0.2 Terabits/in^2 (Tbpsi, thus $0.2 * 10^{12}$ bits per square inch) and some more fundamental barriers for further increase are faced. For increase of data-density the areal space one bit takes on the disk has to decrease. Basic requirements for a bit are that it can be written, that it can be read back without to much errors and that the information is confined for a long enough period (10 years for example). A new harddrive design for higher data-density must fulfill all three requirements at the same time. Currently the dominant noise that appears simultaneously with the desired read signal when reading back recorded information is media noise. The noise in the read signal is caused by random variations in the location of the recorded transitions [2]. The transitions are not straight across the track but forms a zigzag pattern as plotted in figure 1.1. The zigzag pattern reduces the demagnetization energy and with following the grain boundaries also exchange energy is lowered. The intrinsic media signal to noise ratio has been analyzed [3] and is known as the percolation limit. For reliable low error rate the value of the signal to noise ratio has to be above a certain limit. The percolation limit is given by:

$$\left(\frac{S}{N}\right)^2 \propto \frac{W_w \cdot B}{W_g \cdot a} \tag{1.1}$$

With W_w the width of the readhead, B the width of the readpulse, W_g the mean grain size and a the transition width, see figure 1.1.

To lower the bit size $W_w \times B$ while keeping the signal to noise ratio constant the mean grainsize has to be reduced so that the random nature of the grains is averaged out. Mean grainsize in current drives is about 10nm, and much smaller is not possible due to an effect known as the superparamagnetic effect [4]. The superparamagnetic effect is the effect that at a certain grain volume the magnetic energy (KV) becomes too low compared to the thermal energy of a grain (k_bT). Thermal fluctuations ultimately are able to switch the magnetization of a bit, thereby loosing its information. To maintain an average storage time of 10 years the ratio $KV/k_bT \simeq 40$ must be kept. With K the magnetic crystalline anisotropy (a material constant), V the volume of one grain, k_b the Boltzmann constant and T the temperature.

The thickness of the recording medium is limited by the ability of the writehead to produce high field at longer (deeper) distances. Increasing the value of the crystalline anisotropy, K, is not a solution to the superparamagnetic limit. With anisotropy also the coercive field of the grains increase, higher coercive field demands for higher writing fields and higher writing field are not available. Therefore the contradictory need for smaller grains to increase the signal to noise ratio and the the need for larger grains to increase the data confinement time restrains further increase of data density.

Nevertheless some novel approaches already postponed the superparamagnetic limit and might further postpone it in the future. A recent invention from IBM and Fujitsu [5] [6] decreased the impact of the superparamagnetic limit with a new form of recording media. This media consists of two ferromagnetic layers antiferromagnetically coupled by a thin ruthenium layer (referred to by IBM as 'Pixie Dust'). It can be shown that no degradation of the resolution of the readpulse and thus the linear density B in equation 1.1 results from the two antiferromagnetic coupled recording layers in stead of the normal one ferromagnetic layer [2]. The advantage of this double recording layer is that it is double as thick and therefore the grains have a larger effective volume giving them a larger anisotropy energy, $K \cdot V$, and hence smaller lateral grain sizes are possible with the same confinement time. The effective volume is bounded by

$$K \cdot V_1 \leq K \cdot V_{eff} \leq K \cdot V_1 + K \cdot V_2. \qquad (1.2)$$

With tight coupling and alignment of the grain axes the upper limit is approached.

Seagate employs most of their effort in a novel concept where heat assists the magnetic writing by lowering the anisotropy of the bit to be written (HAMR). Recording media with higher anisotropy can now be used without demanding higher writefields because the heating of a bit temporarily lowers the anisotropy during recording. This postpones the superparamagnetic limit to smaller grainsizes. The basic physics of HAMR have been demonstrated in a laboratory setup, but making a practical head requires co-locating the magnetic field and the heated spot. Moreover it has been shown that the heated spot must be approximately equal in size to the bit, necessitating the use of near field optics. Perhaps the biggest obstacle to overcome in implementing the HAMR technology is making a reliable head-disk interface that will enable sufficiently small head-media spacings (HMS) to achieve the necessary resolution. It is projected that at 1 Tbpsi, the HMS will need to be of the order of 5 nm [7].

Another approach for going beyond the limits of perpendicular recording is to make patterned media in which bits consists of isolated islands of magnetic material. Although this approach has been demonstrated at a density of 0.2 Tbpsi with patterns defined by focused ionbeam milling, a commercial realization will require a low cost method for production. Possible approach for patterned media is to use self-ordering arrays of nanoparticles. 6 nm

wide FePt nanoparticles have been demonstrated to self-order and FePt particles can be, in theory, produced thermally stable until a size of 3 nm. The anisotropy of such particles is so high that they could not be written with a magnetic field alone. Thus again pointing to HAMR as a possible solution for future increases of data density.

The use of heat in the HAMR concept implies the use of a rather new and complicating technology in harddrives. Heat is used to lower the crystalline anisotropy but might also influence other parameters of magnetic switching. Besides anisotropy and magnetic moment also the Gilbert damping parameter in the description of magnetic switching might change with temperature. In this thesis a first approach is made to measure the Gilbert damping as function of applied laser heat.

Thiele et al. [8] came with another concept for increasing the anisotropy and therefore potentially decrease the grain size. They showed that a bilayer of FePt/FeRh can form an exchange-spring system where FePt has high anisotropy and high coercivity and FeRh is antiferromagnetic at room temperature but upon heating above the transition temperature becomes ferromagnetic with a large magnetic moment and low anisotropy. When the bilayer is heated above the transition temperature the inplane magnetic moment of FeRh helps the external field to switch the 'hard' FePt layer. This opens intriguing possibilities for HAMR, where the ferromagnetic FeRh assists the heated media to switch while the antiferromagnetic FeRh at room temperature supports the long-time stability. For use in magnetic recording media the time necessary for the FeRh to change its phase from AFM to FM is of crucial importance since I) this gives a limit to the data write speed and II) long term heating of a particular bit also increases the temperature of surrounding grains imposing a smaller data density. In this thesis the time scale at which the phase change occurs is measured.

2 Introduction

In the period April 2003 until July 2004 a traineeship is done at Seagate research in Pittsburgh, PA in the USA as final part for the degree of Master of Science in Applied Physics. Seagate is an harddrive manufacturer and has a research facility in Pittsburgh. Main goal of this department is to investigate novel concepts for magnetic recording in harddrives with the aim to increase data-densities.

Information storage in harddrives is based on the magnetization of small areal parts of a magnetic layer on the surface of a disk. Writing of bits of information is done by magnetizing 'bits' on the disk surface, readback is done with a sensor sensitive for magnetic fields. The so called paramagnetic limit currently restrains harddrive manufacturers from further increase of the data density. To overcome this paramagnetic limit novel concepts have to be investigated. Seagate employs most of their effort in the concept of Heat Assisted Magnetic Recording (HAMR). For HAMR not only magnetic fields are used to write the bits on the disk surface but also a laser pulse is used to first heat the bit to be written. For the design of fast and reliable recording exact knowledge of the dynamics of magnetic switching is of utmost importance. With the HAMR concept heat is introduced for the first time in a magnetic recording device. Although magnetization dynamics are extensively studied, much is still unknown. Moreover, since heat is never used for magnetic recording before, many studies on magnetization dynamics do not involve the influence of temperature.

Magnetization dynamics at constant temperature are described by the Landau Lifshitz Gilbert equation (LLG equation). When a quasi-static temperature is assumed LLG can be used to describe the magnetization in a non-constant temperature. Therefore it is necessary to know the temperature dependence of the individual parameters used in the LLG equation. One of the important parameters in LLG carrying Seagate's interest is the Gilbert damping parameter α. To investigate the influence of laser pulses, temperature and some other external quantities on the value of the Gilbert damping parameter a pulsed laser system is used in a pump-probe setup. For measurement of the dynamics in recording media, the magnetic disk as used in a harddrive, some specific adjustments had to be made. In chapter 3 the pump-probe setup is described.

The LLG equation describes the dynamics of the magnetic moment of an atom, also called the spin of that atom, when the magnetic moment is not in equilibrium with the magnetic external or internal fields. The magnetic moment is in 'equilibrium' when the magnetic energy is minimized. If all mechanisms influencing the energy of a spin are expressed as internal or external fields the minimum energy of the spin is equal to the minimum Zeeman energy, i.e. equilibrium means aligning of the spin with the total of internal and external fields. For the description of macroscopic magnetization the equations for all microscopic magnetic moments must be calculated separately. Macroscopic magnetization dynamics can also be approximated fairly well by assuming one single spin representing the whole magnetization, called isospin approximation. When the magnetization is out of equilibrium it starts to precess around its equilibrium to finally reach equilibrium by a damping process, according to the LLG equation.

When bits are written to the disk in a harddrive, switching of magnetization direction also occurs according to the LLG equation. That means that during the switching process also magnetization precessions occur. The time needed for precessions to damp out influences

the writing speed, because the shape and duration of the writing field needs to be in such a way that it securely switches a bit. With the pump-probe setup magnetization precessions are initiated in recording media proposed for the future HAMR-drive using optical pulses. Although the optical pulses initiate small angle precessions rather than a complete switching of magnetic bits, the measurement of these precessions can be used to describe precession after any kind of excitation.

All processes leading to the damping of precession to a stationary magnetization direction are gathered in the Gilbert damping term in the LLG equation. Gilbert damping is therefore a more phenomenological parameter. Although unraveling of Gilbert damping in all its contributors would be the ultimate goal from scientific point of view, measurement of the effective value of the damping term depending on material properties and external quantities is already a major step forward. Especially from technological point of view the behavior of the total effective damping is useful since it describes the actual time necessary to switch and damp a magnetic bit. The measurement of Gilbert damping depending on pump power, applied field and material properties is described in chapter 4.

Relatively distinct project in the sense of technological implementation is the measurement of the magnetic phase transition in FeRh as described in chapter 5. FeRh is known since 1938 to be antiferromagnetic at room temperatures but ferromagnetic at temperatures above approximately 100°C. FeRh might be used as a layer underneath the HAMR recording layer to help switch the magnetic bits. If, in addition, the phase change in FeRh occurs at a very short timescale the material will be of great technological interest. Besides the time needed to change from antiferromagnetic to ferromagnetic is also of scientific interest. Lots of work is already done to measure and explain the demagnetization process when heating through the Curie temperature [9]. With FeRh we have access to the reversed phenomenon: heating through a transition temperature leads to ordering of the magnetic moments. With the pump-probe setup temporal measurements are described in chapter 5.
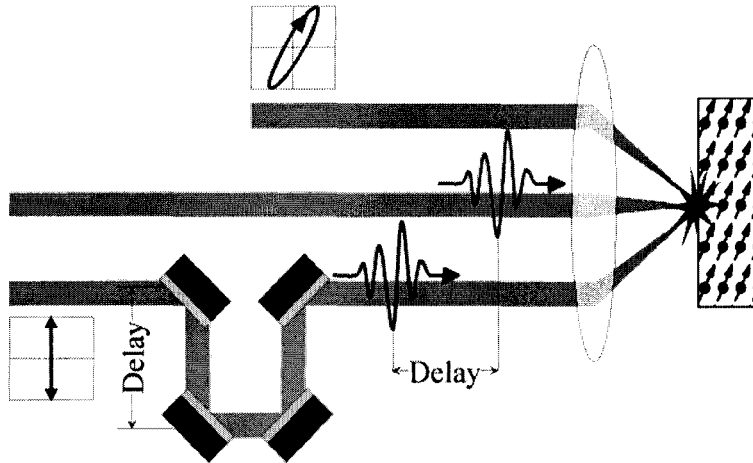
Figure 3.1: General pump probe scheme. An intensive pump pulse excites a magnetic sample, a time delayed weaker probe pulse measures the magnetization through the magneto optical Kerr effect. With scanning the delay of the probe-pulse the temporal relaxation dynamics are obtained.

3 Pump-Probe Technique

In a pump-probe experiment the sample under study is suddenly brought out of equilibrium by a pump pulse, and after a certain time delay the state of the system is measured by a probe pulse. With this technique magnetization dynamics are studied in Perpendicular Magnetic Recording Media (PMR) and FeRh thin film. In this chapter the pump-probe technique is discussed. First the general scheme of a pump-probe experiment is explained in section 3.1. Thereafter calculation of the heat diffusion in the sample for the specific case of this pumping scheme is done in section 3.2. The influence of heat on the magnetization dynamics and the onset of magnetization precession is discussed in section 3.3. The Kerr effect is exploited to measure the magnetization state of the sample at a certain delay. Section 3.4 discusses the Kerr effect and the way it is used for measuring the magnetization in the sample under study. Finally in section 3.5 the practical implementation of the pump-probe scheme is presented and explained in detail. In conclusion some problems and sources of errors are discussed and some recommendations are mentioned.

3.1 General scheme

To gain access to dynamics on ultrafast timescales, i.e. in the order of picoseconds, only a limited number of techniques is available. In this thesis the pump-probe technique is used to study magnetization dynamics in PMR media and FeRh thin film. The basic scheme for pump-probe experiments is given in figure 3.1. A strong and ultrashort laser pulse (pump) is focussed to a narrow spot on the sample and thereby almost instantaneously heats the sample. A weaker and time delayed laser pulse (probe) is focussed to the same spot on the sample. After reflection by the sample rotation and phase-retardation of the polarization

femtosecond
laser pulse
I. Thermal electrons
II. Lattice
electron-phonon
relaxation
g_{ep}
electron
thermalization
excited
electrons
t_{th}
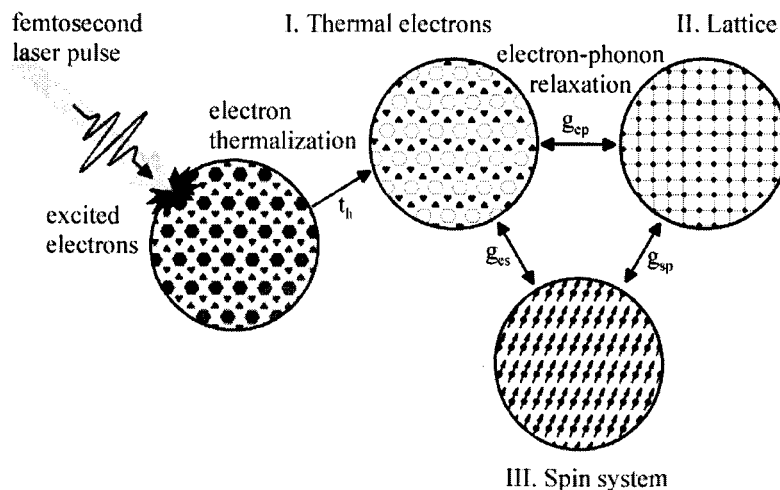g_{es}
g_{sp}
III. Spin system

Figure 3.2: Three temperature model according to Beaurepaire [10]. Excited electrons need to redistribute their energies before an electron temperature is defined (thermalization), then through electron-phonon scattering heat is transported to the lattice, a process typically taking a few picoseconds. Meanwhile energy will also be transported to the third temperature bath, the spin system. All heat fluxes are linearly dependent on the temperature difference.

of the probe pulse is a measure for the magnetization of the sample. At the same time, reflectivity change of the sample, thus intensity change of the reflected probe pulse, is a measure for the temperature. The temporal delay between the pump and probe laser pulse can be adjusted with adjusting the optical path of one of the pulses. By mechanically shifting two mirrors on a track with submicrometer precision, subpicosecond temporal delay resolution can be easily achieved. Important note here is that the technique is not direct, it does not yield the full time-response upon excitation by one pump pulse. Instead, it is a stroboscopic method in the sense that it yields for a certain pump-probe delay an average response. Scanning the delay than provides a full view on the evolution of the magnetic state after excitation.

When the intensive optical pump pulse hits the sample the electrons are excited by the oscillating electric field of the optical pulse. After excitation the electrons thermalize through a process of electron-electron scattering, which typically takes less than 1 ps. After thermalization of the electrons the heat has to be conducted to the phonons, the lattice. Beaurepaire et al. [10] even proposed a third system, the spin system. With these three systems, three temperature baths are defined and Beaurepaire introduced a phenomenological description of the interaction of electrons, phonons and spins with the three temperature model.

Figure 3.2 presents a conceptual picture of the three temperature model. After thermalization three temperatures can be defined. Each system or temperature bath has its own temperature, thermally separated from the other systems. By electron-phonon collisions, electron-spin interaction and phonon-spin interaction heat is transferred between the three systems to obtain a new thermodynamic equilibrium. For this heat transport temperature difference is the driving force, i.e. the heat flux is linear dependent on the temperature difference. Typically all three samples are in thermodynamic equilibrium after a few picoseconds. For the study of magnetization dynamics in relation to temperature, the spin temperature is the temperature of importance since the magnetization is carried by the spins.

After the pump pulse the sample cools back to environmental temperature by diffusion
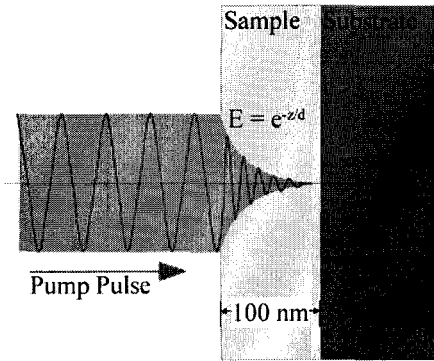
Figure 3.3: The electric field of a pump pulse entering the sample surface and penetrating it with a penetration depth d. The distribution of the energy deposited by the pump pulse will be exponential with sample depth and Gaussian in lateral directions.

of heat into the sample. This cooling process is a slow process compared to internal heat transport processes and therefore occurs with thermal equilibrium between the subsystems. In the next section cooling by diffusion into the sample is discussed.

3.2 Diffusion

With the pump-probe experiment the temperature decay of the sample after it has been heated with a pump pulse can be probed. From the temporal results on the sample temperature a diffusion constant can be determined. In this section a solution of the diffusion equation will be presented. With fitting of this solution in the pump-probe reflectivity data, the diffusion constant can be calculated.

Heating of the sample is done by a pump pulse in the near infrared regime (800nm). A pulse of approximately 80 femtoseconds heats the sample to a certain temperature. Heat diffusion, both perpendicular and lateral, will cool the sample back to environmental temperature in typically 200 ps. A schematic drawing of the heating mechanism is given in figure 3.3. The electric field of a pump pulse enters the sample and penetrates it with a certain penetration depth δ_0. The initial temperature rise caused by this pump pulse will be accordingly distributed over depth:

$$T_0(z) = T_{00} \cdot e^{-z/\delta_0}, \tag{3.1}$$

with T_0 the temperature rise at $t = 0$, δ_0 the penetration depth, typically in the order of 30nm, z the depth into the sample and T_{00} the temperature on the surface ($z = 0$) at $t = 0$. The lateral distribution of temperature is in the order of $3\mu m$, the size of the focussed light on the sample. Therefore pure perpendicular diffusion of temperature will describe the cooling process appropriately. In case of a homogeneous medium with a constant diffusion coefficient the one dimensional diffusion equation is given by:

$$\frac{\partial T}{\partial t} + D\Delta T = 0, \tag{3.2}$$

with D the diffusion coefficient [m^2·s^{-1}] and T the temperature difference with the environment [K], and Δ the Laplace operator (∇^2). In the case of a delta shape initial temperature distribution $\delta(z - z_0)$ at $t = 0$ the solution on $z \in \mathbb{R}$ of this equation can be obtained using

Fourier transformation. The diffusion equation in the Fourier domain:

$$\frac{d\tilde{T}(k,t)}{dt} + k^2 D\tilde{T}(k,t) = 0, \tag{3.3}$$

with

$$T(z, z_0, t) = \frac{1}{\sqrt{2\pi}} \cdot \int_{-\infty}^{\infty} \tilde{T}(k,t) \cdot e^{ik(z-z_0)} dk. \tag{3.4}$$

Solution of this ordinary differential equation is:

$$\tilde{T}(k,t) = \tilde{T}_0(k) \cdot e^{-k^2 Dt}, \tag{3.5}$$

with $\tilde{T}_0(k)$ a constant factor which can still depend on k. To obtain $\tilde{T}_0(k)$ the start condition is substituted. The Fourier transform of $\delta(z)$ is $\mathcal{F}(\delta(z)) = 1/\sqrt{2\pi}$ and the variable shift in the time domain results in a multiplication in the Fourier domain:

$$\mathcal{F}(\delta(z - z_0)) = \frac{1}{\sqrt{2\pi}} \cdot e^{-ikz_0}. \tag{3.6}$$

Substitution of $t = 0$ in (3.5) results in:

$$\tilde{T}_0(k) = \frac{1}{\sqrt{2\pi}} \cdot e^{-ikz_0}, \tag{3.7}$$

and thus:

$$T(z, z_0, t) = \frac{1}{2\pi} \cdot \int_{-\infty}^{\infty} e^{-k^2 Dt + ik(z-z_0)} dk = \frac{1}{2\sqrt{\pi Dt}} e^{-\frac{(z-z_0)^2}{4Dt}} \tag{3.8}$$

is the response to a delta pulse. This solution is also called the source solution to the diffusion problem. The solution to a general initial temperature distribution $T_0(z, t = 0)$ can be obtained by convolution:

$$T(z, t) = (T_0(z_0) * T(z, z_0, t)) = \int_{-\infty}^{\infty} T_0(z') \cdot T(z, z', t) dz'. \tag{3.9}$$

With a symmetrical function T_0 around $z = 0$ one obtains the diffusion in a semi-infinity long wire, thermally isolated at $z = 0$.

As noted before the initial temperature distribution can be taken as exponential according to 3.1. But one can also argue that due to the finite time necessary to heat the sample (approximately 80 fs), due to a non equilibrium electron temperature and due to ballistic electrons the temperature profile will be Gaussian very soon after heating the sample [9]. Gaussian initial temperature rise assumption is given by:

$$T_0(z) = T_{00} \cdot e^{-\frac{z^2}{2\sigma^2}}, \tag{3.10}$$

with $\sigma = \delta_0/\sqrt{2}$. Fortunately the response to a delta pulse heating of the sample is already a Gauss (cf. Eq 3.8), broadening in time. Thus using 3.8 shifted in time over $t_0 = \delta_0^2/4D$ results in the response on a Gaussian temperature distribution with initial width δ_0:

$$T(z, t) = \frac{\delta_0}{\sqrt{4Dt + \delta_0^2}} e^{-\frac{z^2}{4Dt + \delta_0^2}}, \tag{3.11}$$
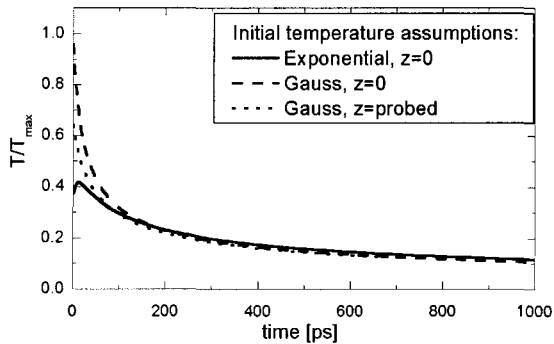
Figure 3.4: Diffusion according to the two different initial temperature assumptions (3.1,3.10) at two different depths in the sample and also the probed average for the Gaussian initial temperature.

where the result is multiplied with $2\sqrt{\pi}\delta_0$ to obtain $T = 1$ on the surface at $t = 0$. This result is exactly the same as one would obtain by integrating the source solution with an Gaussian initial temperature profile according to equation 3.9.

The probe penetrates the sample similar to the pump as given by equation 3.1. After reflection the probe caries averaged information of the sample on different depths, where the probe sensitivity exponentially dependents on the depth into the sample. Thus when a pump-probe experiment is done to obtain the temperature decay due to diffusion not only the the surface temperature will be observed but a weighed average of temperatures over a certain depth into the sample. The expected result of a pump-probe temperature measurement will thus be the average of equation 3.11 over a depth range with the probe intensity as a weighing factor:

$$T_{probed} = \int_0^\infty T(z,t) \cdot \frac{\sqrt{2}}{\delta_0} \cdot e^{-z\sqrt{2}/\delta_0} dz = \sqrt{\frac{\pi}{2}} e^{\beta\gamma^2} \left(1 - \mathrm{erf}(\gamma\sqrt{\beta}) \right), \qquad (3.12)$$

with $\beta = Dt + \delta_0^2/4$ and $\gamma = \sqrt{2}/\delta_0$. For large $\gamma\sqrt{\beta}$ equation 3.12 can be approximated[1]:

$$T_{probed} \cong \frac{1}{\sqrt{2}\gamma\sqrt{\beta}} = \frac{\delta_0}{\sqrt{4Dt + \delta_0^2}}. \qquad (3.13)$$

Note that this result is exactly the surface temperature as given by equation 3.11. Thus the fact that the probe has an exponential sensitivity with the depth has only effects on the reflectivity measurement during the first 30ps. Direct solution of (3.9) with an exponential initial temperature (3.1) gives:

$$T(z,t) = \frac{1}{2} e^{\frac{Dt - \delta_0 z}{\delta_0^2}} \left(1 - \mathrm{erf}\left(\frac{2Dt - \delta_0 z}{2\delta_0\sqrt{Dt}} \right) \right) + \frac{1}{2} e^{\frac{Dt + \delta_0 z}{\delta_0^2}} \left(1 - \mathrm{erf}\left(\frac{2Dt + \delta_0 z}{2\delta_0\sqrt{Dt}} \right) \right). \qquad (3.14)$$

Results with both initial temperature assumptions, the exponential as well as the Gaussian temperature for $t = 0$, are plotted as function of time for $x = 0$ (Equations 3.14 and 3.11) together with the result for the probed temperature (Equation 3.12) in figure 3.4. Because the difference in results are not large (smaller than 13% after 10 ps) the simplest equation is taken for fitting of the measurement data, equation 3.11, as will be described in chapter 5.
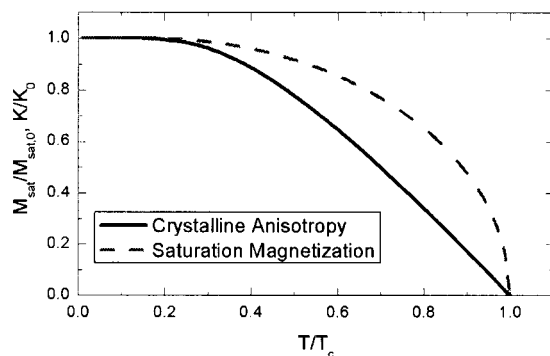
Figure 3.5: The temperature dependence of the saturation magnetization (M_s) and crystalline anisotropy constant (K) as calculated by Wu et al. [11].

3.3 Magnetization Dynamics

When the sample is heated by a pump pulse in a pump-probe experiment the saturation magnetization decreases and also the anisotropy constant, K, decreases. Calculation by Wu et al. [11] of the value of M_s and K relatively to the absolute zero values is presented in figure 3.5 for temperatures normalized to the Curie temperature.

With temperature (spin-temperature) the length of the magnetization vector thus changes. The direction of the magnetic moment in the dynamic case is given by the The Landau Lifshitz Gilbert (LLG) equation:

$$\dot{\mathbf{M}} \cdot (1 + \alpha^2) = -\gamma_0 (\mathbf{M} \times \mathbf{H}) - \frac{\alpha \gamma_0}{|\mathbf{M}|} \cdot (\mathbf{M} \times (\mathbf{M} \times \mathbf{H})). \tag{3.15}$$

with α the dimensionless Gilbert damping, $\gamma_0 = \frac{g \mu_B \mu_0}{\hbar} = 221 \cdot 10^3 [\text{mA}^{-1}\text{s}^{-1}]$ and $\mathbf{H}$ the total effective field [A/m]. The first term on the right hand side, the Landau Lifshitz term, describes the precessional motion, the magnetization will precess around the net applied field. The second term, the Gilbert term, describes the damping. The precession is damped and after a certain amount of precessions the magnetization will end aligned with the net applied field. Since the Zeeman energy is lowest when the magnetization is aligned with the applied field, this is the equilibrium direction. Note that LLG will not affect the length of the magnetization vector, $\frac{\partial |\mathbf{M}|}{\partial t} = 0$, the length only changes with temperature.

The total effective field as introduced here consists of three elements:

$$\mathbf{H} = \mathbf{H}_{\text{ext}} + \mathbf{H}_{\text{demag}} + \mathbf{H}_{\text{anis}}, \tag{3.16}$$

the externally applied field, $\mathbf{H}_{\text{ext}}$, an imaginary field (or demagnetizationfield) representing the shape anisotropy, $\mathbf{H}_{\text{demag}}$ and an imaginary field (or anisotropyfield) representing the crystalline anisotropy, $\mathbf{H}_{\text{anis}}$.

Shape anisotropy is related to the minimization of energy by minimizing the strayfield outside the magnetic material. The shape anisotropy or demagnetization field will in principle point perpendicular to the film surface and opposite to the magnetization direction:

$$\mathbf{H}_{\text{demag}} = (0, 0, -\mathbf{M}_z). \tag{3.17}$$

---

[1]Error made is $\leq 5\%$ when $Dt \geq 0.66 \cdot \delta_0^2$, i.e. for $t \geq 30\text{ps}$ for typical values of D and δ_0.
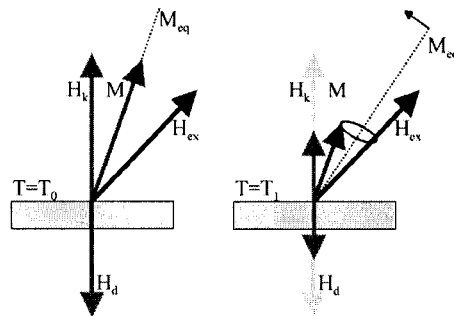
Figure 3.6: Mechanism of precession initiation for PMR samples. The magnetization will be in equilibrium when it points in a certain direction somewhere between the external field, applied under an angle of 45 degrees, and the perpendicular anisotropy. After instantaneous heating by a pump pulse, the magnetization and the anisotropy will quench while the external field remains constant. The new equilibrium magnetization now lays closer to the external field direction and since the magnetization direction itself does not change instantaneously it is not in equilibrium anymore. The magnetization starts to precess around the new equilibrium. After excitation the sample slowly cools back to its initial temperature by diffusion. The magnetization and anisotropy recover during this process, rotating the equilibrium back to its initial direction. Thus the magnetization precesses around an equilibrium which itself changes in time.

Crystalline anisotropy is related to the crystalline structure, depending on the structure magnetization is energetically favored in a certain direction. In a granular film small deviations from this direction may occur at the edges of the grains. Granular films normally have a spreading of the anisotropy over the grains of a few percent. The PMR samples used in this work have, as is in the name, crystalline anisotropy fields perpendicular on the surface and thus, in rest, perpendicular magnetization.

In figure 3.6 the all optical excitation mechanism of precessional motion in a Perpendicular Magnetic Recording (PMR) sample is explained [12]. The raised sample temperature due to the pump pulse causes a quenching of the magnetization and the anisotropy. Since the external field is constant and under an angle with the magnetization the new equilibrium magnetization direction is closer to the external field direction. Due to the instantaneous heating and the almost instantaneous quenching of magnetization the magnetization is not in the equilibrium direction anymore and will start to precess around the equilibrium. During the cooling of the sample the magnetization recovers and the equilibrium direction moves back to its initial direction. Thus the magnetization vector precesses around an equilibrium, which itself changes its orientation during the process and meanwhile also the length of the magnetization vector increases.

3.4 Kerr Effect

The relaxation dynamics are probed with a laser light pulse after it is excited with a strong pump pulse. Magneto-optical Kerr effect (MOKE) is the exploited effect for measuring the magnetization at certain delay after the pump pulse have arrived. Light that is reflected from a magnetized surface experiences a polarization rotation and a phase retardation, called rotation and ellipticity, linearly dependent on the magnetization strength. The Kerr effect is closely related to the Faraday effect, here polarization rotation takes place by transmission of the electromagnetic beam rather than by reflection. Contrary to the Kerr effect which
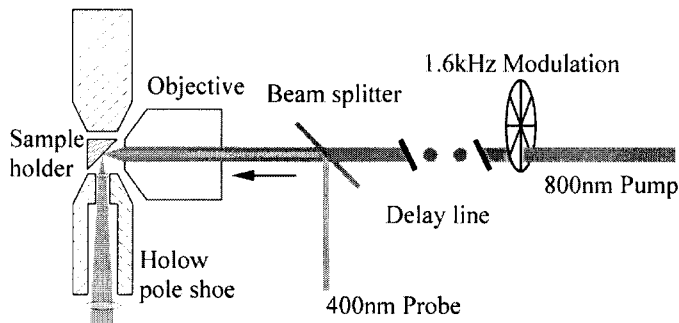
Figure 3.7: For physical implementation of the pump probe scheme some more practical compromises have to be made. To prevent the granular perpendicular recording media to break into domains of different magnetization and to be able to saturate the sample in one direction at relatively low fields an angle between the external field and the sample surface is preferred. Small sizes of the focussed spot requires objectives with short workingdistances, requiring small magnet-poles, or a large gap between the poles both leading to lower fields. To maintain an homogeneous field as much as possible the hole in the pole must be small, while for collimation the the diameter must be large depending on the workingdistance.

is primarily observed on magnetic materials the Faraday effect is also often exhibited by nonmagnetic materials.

Three contributions to the Kerr rotation can be distinguished, the longitudinal, transversal and polar Kerr effect. Polar Kerr effect is the rotation and elipticity gained due to the magnetization component normal to the sample surface. Longitudinal Kerr effect is due to the component of magnetization in the sample plane and in the plane of incidence. Transversal Kerr effect is sensitive to the magnetization in the sample plane and perpendicular on the plane of incidence. The polar Kerr effect is the most sensitive to the magnetization, longitudinal and transverse are generally 100 and 1000 times less sensitive.

In the measurements presented here transversal and longitudinal effects are assumed to be negligible and only Kerr rotation is measured. This is done using a linear polarizer and a Wollaston prism. The polarizer polarizes the probe beam before it is reflected by the sample. The Wollaston prism splits the beam in two perpendicular components of polarization, the intensity of both beams is detected with two photodiode detectors. With substraction of the two detector signals the Kerr rotation is obtained while addition of the two signals gives the reflectivity. A detailed analysis of the separation of reflectivity and Kerr rotation is given by Koopmans [13].

3.5 Setup

To measure the pump induced magnetization dynamics and temperature the transient Kerr rotation and reflectivity must be separated from the overall reflectivity and polarization. This is done by modulating the pump beam with a mechanical chopper. With a chopping frequency ($\simeq 1.6$kHz) much lower than the repetition rate of the laser pulses ($\simeq 8$MHz), to prevent for aliasing effects. With a lock in amplifier the transient reflectivity and Kerr rotation is now measured. The transient difference of the signals on both photodiode detectors is given by:

$$S_{\text{Dif}} = \Delta(R\Theta) = R\Delta\Theta + \Theta\Delta R + \Delta R\Delta\Theta, \tag{3.18}$$

where 'Δ' means the transient signal, R is the reflectivity and Θ is the Kerr rotation and proportional to the polar component of the magnetization. The relative change in reflectivity in ferromagnetic samples is generally much smaller than the relative change in Kerr rotation, $\Delta R/R \ll \Delta\Theta/\Theta$, therefore only the first term in equation 3.18 contributes to the measured signal.

The sum of the detector signals directly leads to the transient reflectivity (R), with the summing of the two polarization directions all polarization sensitivity is excluded and only the transient reflectivity remains:

$$S_{\text{Sum}} = \Delta R. \tag{3.19}$$

Recording media exist of a granular magnetic film, grains are typically in the order of 10nm in diameter and therefore magnetization dynamics are probed over a large number of grains. Because of the granular structure the external field must be applied under an angle with the surface. If the field is applied in the sample plane individual grains will randomly switch at elevated temperatures, causing a zero net magnetization.

For an external field under an angle of 45° a relatively small tabletop electromagnet with adjustable poles is used. To obtain high and homogeneous fields together with high focussation of the laser beam and good collimation after reflection on the sample some more practical compromises had to be made. A Nikon microscope objective with a numerical aperture of 0.7 with a relatively long working distance of 8mm is used. With especially machined pole shoes a small pole gap is made while leaving enough room for the objective to approach the sample without making physical contact between the poles and the objective.

Collimation of light after reflection on the sample is done with a small lens with a focal length of 7mm and a diameter of 6mm. The collimator is mounted at the poleshoe of the hollow pole. The gap between sample and poleshoe is more than the working distance of the collimator and therefore a second collimator is necessary after the beam traveled through the magnetpole. See figure 3.7

With a beam splitter the two beams, the pump and the probe, are combined together and directed to the center of the objective. The focussed spots on the sample of the two beams will overlap when both beams are exactly parallel. The overlap can further be fine-tuned with adjusting the angle of the beamsplitter, and thus the angle of the probe beam, while maximizing the transient reflectivity signal.

To make sure that the probed area on the sample has an highly homogeneous temperature an additional positive lens with a focal length of 2m is added just before the beamsplitter in the pump beam path. The slightly diverging pump beam causes a slight defocussing of the pump spot on the sample, making the pump spot slightly larger than the probe spot to minimize the temperature gradient over the probed area.

Because the delayline might affect the beam alignment and because the retroreflector used was best suited for the 800nm wavelength the pump beam is delayed in stead of the probe beam. This gives, with a fixed extra delay for the probe, equivalent time delays between pump and probe pulse.

With a Ti:Sapphire laser 80 femtosecond long pulses are generated with an energy of 20nJ at a wavelength of 800nm. Pulses are generated at a repetition rate of 80MHz. With a Second Harmonic Generation crystal (SHG-crystal) a blue weaker pulse with a wavelength of 400nm is generated at each original (red) pulse, resulting in two, synchronized, pulse trains: intense red pulses (pump) and weaker blue pulses (probe).

3.6 Discussion and Recommendations

Although special care is taken to make sure that the pump spot on the sample is larger than the probe spot it is still not exactly known how large both are and if they are really exactly centered. Even in the ideal case of exactly centered perfect circular spots there exists some temperature gradient in the probed area, thus the probed signal is a weighted average of magnetization dynamics over a certain temperature range.

Because the Kerr rotation as well as the reflectivity are affected by thermal excitation both are present in the obtained signals.

Although, as said in section 3.4, the relative reflectivity is generally much smaller than the relative Kerr effect aiming for deviations from the expected signal might occur. Especially shortly after pump excitation the reflectivity changes can be reasonably large.

An interesting point of improvement might be a polarization modulation of the probe beam. Then Kerr rotation and elipticity can be recorded simultaneously. Depending on the material under study one of them will be most sensitive to the magnetization and can be chosen for further analysis.

Although the scheme with two different wavelengths for the pump and the probe has the strong advantage that they can be easily separated before detection takes place it also has a disadvantage. The Second Harmonic Generation (SHG) crystal producing the probe beam has the problem that the resulting beam is not as nicely parallel as the original beam. It can therefore not be focussed as well as in case the that no SHG crystal is used.

4 Precession Damping in Perpendicular Recording Media

To continuously increase the data write speeds of future harddrives better control and knowledge of the damping of precession is necessary. Currently data rates in laboratory demonstrations[1] are around 1 Gbps (Giga bit per second) which means writing times of 1 ns. Increase of media damping helps to reduce the back switching caused by the media magnetization precession, hence reduce the field duration needed [14]. In addition, one of the future ideas to achieve higher data densities, the HAMR drive, will make use of heat to write the magnetic bits. Important question for this future scheme is how the Gilbert damping term behaves at changing temperatures.

Therefore precession measurements are done using the magneto optical Kerr effect on potential HAMR media with perpendicular anisotropy. From the resulting Kerr graphs the Gilbert damping term is deduced and plotted against the pump power. With the pump the sample gets heated and this triggers the precession. As a function of increasing pump power the sample temperature as well as the amplitude of precession increases.

To find out what the effect of excitation, or precession amplitude, is on the Gilbert damping also measurements are done with varied applied field. Precession amplitude as well as Gilbert damping are plotted against external applied field.

For the design of the final HAMR medium various parameters can be adjusted to get an optimal damping, but the effect on the damping of most parameters is unknown. Therefore Gilbert damping as a function of one of the media parameters, the exchange coupling or doping level, is also measured. Exchange de-coupling between the grains is obtained by adding a non magnetic element during the sputtering process, which has a preference to grow on the grain boundaries. The higher the concentration of this non-magnetic element during the sputtering process the lower the exchange coupling between grains.

The Gilbert damping term as given in the LLG equation 3.15 is a rather phenomenological term. In reality many channels for spin damping are possible. Moreover due to the assumption of a strong exchange interaction, discrepancies between the theory of Landau-Lifshitz and reality are internalized in the Gilbert damping. [15].

Tserkovnyak et al. predicts that the Gilbert damping will increase when a normal metal layer is in the vicinity of the ferromagnetic layer [16]. Magnetization precession in the ferromagnetic film will transfer spins into the adjacent normal metal layer, this spin pumping slows down the precession corresponding to an increased Gilbert damping.

Spargo et al. [17] emphasized the shape effects on switching behavior of grain-size magnetic elements, making damping somewhat different from isospin when dealing with average damping over a full grain.

Wu et al. [18] observed a dramatic field dependence of the Gilbert damping in permalloy dots excited with external field pulses. The damping decreases with increasing applied field.

In this chapter results on a series of HAMR samples are presented. An overview of the HAMR sample set and their properties is given in section 4.1. With the pump-probe setup precessions are triggered and measured in the perpendicular HAMR samples, results

---

[1]Data rate in commercially available products is currently about 500 Mbps.
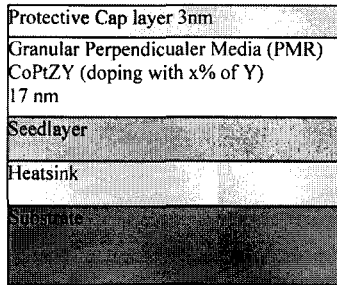
Figure 4.1: Sample structure of the HAMR samples as used for the precession damping measurements. The volume percentage of element Y is varied over the sample set. The size of the grains is approximately 10nm. Elements Y and Z are nonmagnetic elements, for confidentially reasons they are noted as Y and Z here.

Table 4.1: Media parameters of the sample set used for Gilbert damping measurements. The percentile volume of doping element Y in the recording layer is varied over the sample set. This also causes the change in coercivity, nucleation field, and squareness. Coercive field is defined as the field where the hysteresis crosses the zero magnetization line. Nucleation field is defined as the intersection of the slope and $M = 1$. The squareness is defined as the ratio of remanence and saturation magnetization ($S = M_r/M_s$).

Disc/Sample No.	7B	20B	17B	14B	11B
Doping level (volume percentage of Y)	0.00	0.20	0.35	0.50	0.65
Coercivity H_c [kG]	2.12	5.83	5.79	5.69	3.89
Nucleation field H_n [kG]	−1.30	−1.80	−1.08	−0.65	1.37
Squareness S	1.00	0.99	0.97	0.94	0.70

thereof at different pump powers and different external fields are presented in section 4.2. The LLG equation is simulated with a fitting of the reflectivity as input for the temporal temperature profile. Since LLG does not account for temperature changes a quasi static temperature is assumed. Comparison between measurement and simulation with appropriate media parameters reveals the Gilbert damping parameter for each precession measurement. Section 4.2.1 is devoted to the explanation of the simulation and comparison procedure. In section 4.2.2 the Gilbert parameters of all precessions are collected and plotted against the pump power. In section 4.2.3 the Gilbert dependency on applied field is discussed. To compare the results with a less complicated case, the same measurements are also done on ordinary nickel thin film. In section 4.2.4 damping results on nickel film are compared with the media damping results. Finally in the conclusion all results are evaluated and compared.

4.1 Samples

HAMR media samples are fabricated using a sputtering process. In order to measure the dependence of the Gilbert damping on grain exchange decoupling, a sample set with variable exchange decoupling is created. The most recent version of the HAMR media is taken as the base design. Exchange decoupling between the grain elements is obtained by doping the sputtering plasma with a non-magnetic element[2] during fabrication. With increasing doping the non-magnetic boundary layer between the grains increases and therefore exchange

---

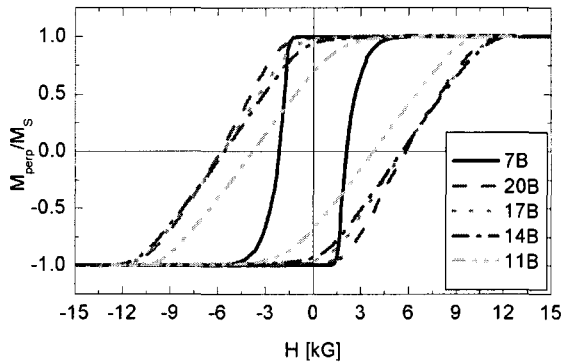[2]The element is confidential and is in this thesis denoted as Y.

Figure 4.2: Hysteresis curves of the HAMR Media with various exchange, with fittings to these curves the sample parameters as presented in table 4.1 are obtained.

coupling decreases. See figure 4.1 for a schematic view of the sample structure. The heatsink is a typical part of the HAMR media design. Since HAMR will make use of heat to write the magnetic bits a method to remove the heat from the recording layer must be implemented in the design. Currently a layer of a good conducting metal is used as the heatsink. The seed layer works as a formatting underlayer, with this seed layer the recording layer will directly grow in a grain structure. If there is no doping during sputtering of the recording layer it will still grow in a grain structure, however the border between the grains will also be filled with magnetic material. Therefore the sample grown without doping has a continuous magneticlayer but the magnetic domains might still be affected by the grain like growing process caused by the seed layer. In table 4.1 an overview of the measured samples is given with the magnetic properties as measured with a Polar Kerr looper (home built). The polar Kerr effect is measured as function of the field. The field is applied in the easy axis direction, thus perpendicular to the media disc. With a field sweep rate of about 1000 Oe/s. In figure 4.2 the hysteresis measurements are presented, fitting of those hysteresis curves gave the media parameters as given in table 4.1[3].

As can be seen in table 4.1 the coercivity strongly increases when the sample structure goes from continuous magnetic film (zero doping) to the granular film. Within the granular films, the coercivity decreases with increasing doping. From the nucleation field it can easily be seen that with the highest doping the media properties change dramatically, suggesting a complete structure change at a doping of 0.65%.

4.2 Results

Precession measurements are done using the pump probe setup as explained in chapter 3 with the external field under an angle of 45 degrees with the sample plane. The pulse repetition is set to 8MHz and the in phase component of the lock-in amplifier is recorded as the Kerr signal (difference of two the detectors) and Reflectivity signal (sum of the two detectors). The Kerr signal turned out to be large enough to be interpreted directly without taking the difference between positive and negative external field. Measurements are done at positive and negative field, which should give equivalent results and therefore can be used for averaging and as a check to notice errors in the measurement technique.

In figure 4.3 until 4.5 a selection of the precession data taken is shown. In the right panes transient reflectivity is plotted against the time. Reflectivity can be assumed linear with

---

[3]Measurement and fitting of these media characteristics are done by Ganping Ju.
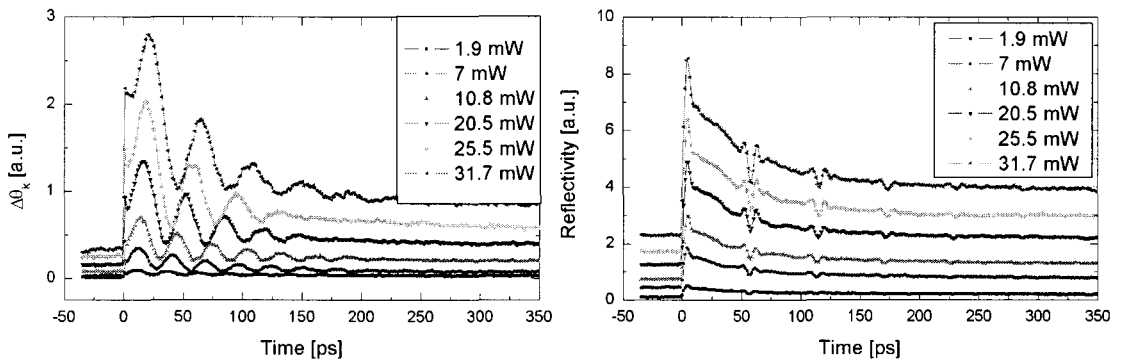
Figure 4.3: With the pump probe setup Kerr rotation (left pane) and reflectivity (right pane) are recorded simultaneously. Measurements are done at about 20 different pump powers with a field of 8kG in both directions on all 5 samples. Here a selection is shown of the precession data and the accompanying reflectivity data, taken with −8kG on the 0% doping sample. Clearly visible is the precession, even at the lowest pump powers. The small wiggles in the reflectivity each 50ps are probably due to sound waves bouncing up and down in the sample.

temperature, hence the temporal behavior of the reflectivity is established by the diffusion equation. Superposed on the linear temperature dependence of the reflectivity small wiggles are seen. Those wiggles are due to sound waves induced by the crystal expansion following the instantaneous heating with the pump pulse. Reflection of the sound wave at deeper sample layers, causes the repetitive appearance every 50ps. In the left panes transient Kerr rotation ($\Delta\theta_k$) is plotted against the time. This Kerr rotation is recorded simultaneously with the transient reflectivity and reflects the magnetization component perpendicular to the sample plane. The sinusoidal behavior, thus, is the one dimensional mapping of a three dimensional precession of the magnetization. Superposed on that precession is the decrease of the magnetization strength due to the temperature dependence of $M_S(T)$ and a decrease of the perpendicular component due to the rotation of the equilibrium magnetization direction. In this measurement only absolute transient Kerr rotation is measured, therefore a decrease in $|\mathbf{M}|$ results in a increase in the transient Kerr measurement. Overall the transient Kerr rotation reflects a convolution of the temperature diffusion and the temperature dependence of $\mathbf{M}$, the rotation of the equilibrium magnetization direction and one spatial component of the precession.

In the pump-probe setup the pump power can easily be adjusted between adjacent measurements without disturbing the optical alignment and thus without affecting other parameters. In figure 4.3 a selection of the about 20 precession measurements is shown. With pump power also the induced reflectivity increases, as expected. Moreover also the background temperature increases considerable as can be seen on the reflectivity at negative time delay, at a pump power of 7mW the background temperature is already comparable with the maximum temperature reached with a pump power of 1.9mW.

Harder to accomplish is to change the applied field without disturbing the optical alignment. When the applied field changes, the temperature of the magnet coils also change which induces all kinds of small shifts in the optical alignment. To prevent for coil temperature induced alignment shifts long temperature equilibration times are regarded at moderate fields. When also the measurements at the highest and lowest fields are performed in a short time, the temperature shift could be kept reasonable. Figure 4.4 shows the data at two
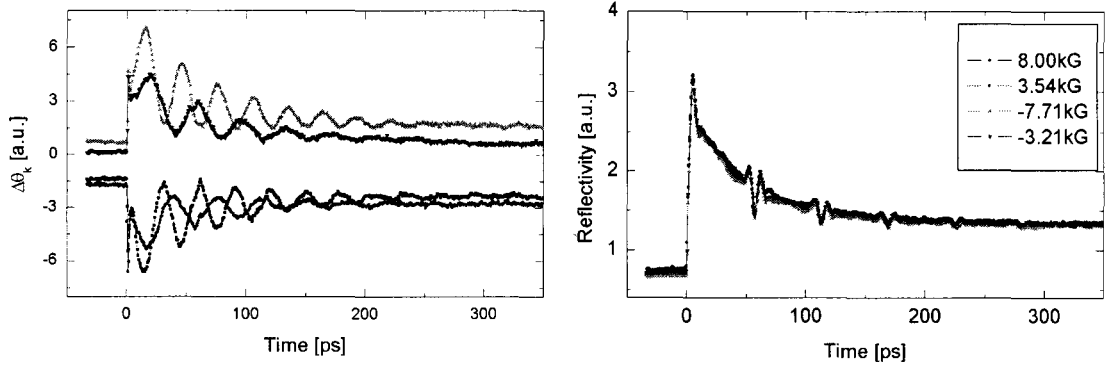
Figure 4.4: Also field dependent measurements are done on all 5 samples at a fixed pump power of 10.8mW, here a selection of some fields is shown together with the reflectivity data. It turned out to be hard to take a complete set of data without changing the setup alignment slightly with the applied fields, the nice overlap of the reflectivity curves in this set shows that the alignment was not affected.
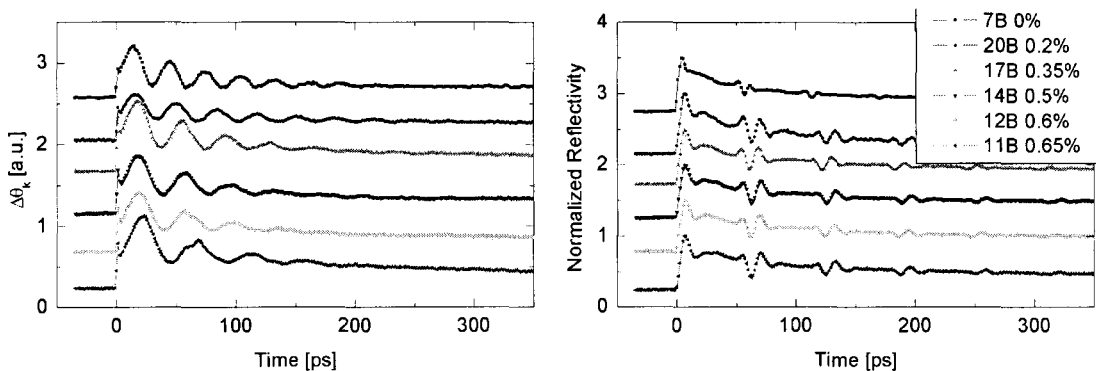

Figure 4.5: One precession measurement on each sample at 8kG and 10.8mW pump power. Between two samples the alignment of the pump probe setup is heavily affected, resulting in more or less collected light after realigning and thus resulting in higher or lower signals, still the normalized reflectivity gives nice reproducable graphs.

different fields in both directions. In total measurements are done at approximately 20 different fields. As can be seen in the reflectivity the alignment was barley changed during the measurements, as required. Moreover, this set of reflectivity curves shows that non of the features in the reflectivity is of magnetic origin, since the size as well as the direction does not change with field strength or direction.

To change the sample in the pump-probe setup the magnet, sample holder and focussing objective had to be demounted. Therefore realignment of the optics is necessary after each sample change. Because the amount of light collected on the detectors is very sensitive to the exact path traveled, the alignment and thus the signal height is never the same for two different samples. In figure 4.5 precession data with 8kG applied field and 10.8mW pump power on the six different doping samples is presented, here the reflectivity data is normalized.
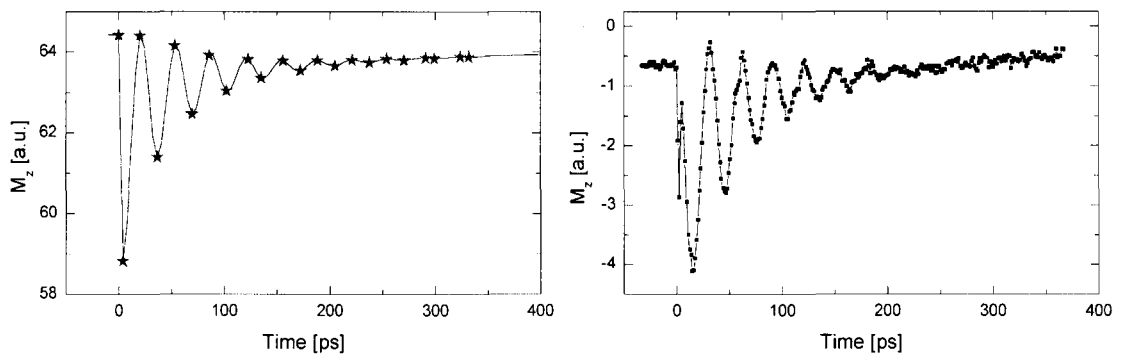
Figure 4.6: Left: Simulation of the magnetization precession after heating 100K, constants used: $M_S = 1\mathrm{MA/m}$, $K = 400\mathrm{kJ/m^3}$, $T_0 = 50\mathrm{K}$, $H_0 = 8\mathrm{kG}$, $t_0 = 1.1284\mathrm{e}{-}11$, $T_C = 827$, $\alpha = 0.1$. Stars indicate the maxima of the precession as found by the fitting program. Right: Kerr measurement of the magnetization at 10.8mW pump power and +8kG on sample 7B, 0% Doping.
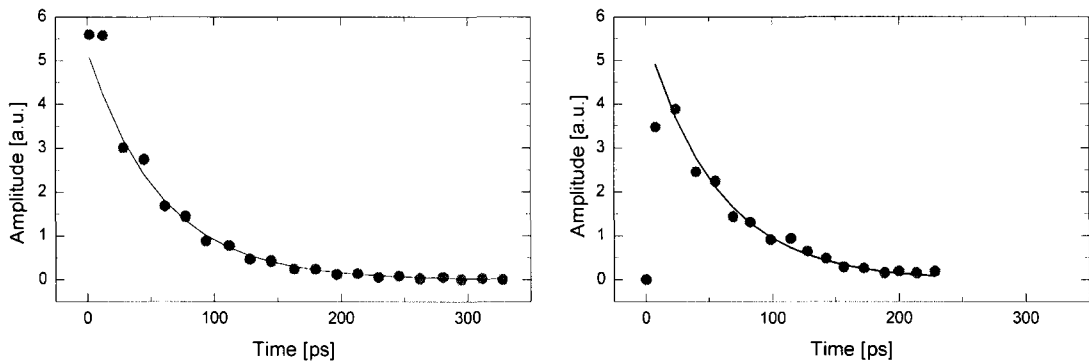

Figure 4.7: Left: Precession amplitude of the simulation and a fitting of an exponential function to it ($\tau = 57.3\mathrm{ps}$). Right: Amplitude of precession in the measurement and a fitting to it, ($\tau = 56.5\mathrm{ps}$)

4.2.1 Extraction of Gilbert Damping Parameter from Measurements

Magnetization dynamics at constant temperature are described by the phenomenological Landau Lifshitz Gilbert (LLG) equation 3.15. The physical solution for a thin film with inplane magnetization, zero crystalline anisotropy and perpendicular applied field is given in equation 4.1 [19]. Here a small excitation from equilibrium is assumed. xyz-components refer to the axis as defined in figure 3.3 in chapter 3.

$$M_x = -M_s, \tag{4.1}$$
$$M_y = M_s \cdot \xi \cdot d\Theta \cdot e^{-t/\tau} \sin(\omega t + \phi),$$
$$M_z = -M_s \cdot d\Theta \cdot e^{-t/\tau} \cos(\omega t),$$

with $d\Theta$ the excitation angle, τ the time constant describing the damping process [s], ω the precession frequency [rad/s], ξ ellipticity due to demagnetization and ϕ a dephasing factor [rad].

To explain the ellipticity in the precessional behavior, not to be confused with the el-
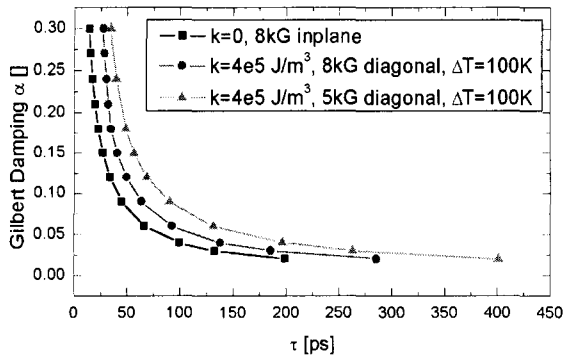
Figure 4.8: Relation between the exponential timeconstant in the precession amplitude and the Gilbert damping constant as it appears in the LLG equation. For the simple case of inplane field and zero crystalline anisotropy an analytical relation is used for the plotted relation (squares), for the more complex case of a diagonal field and non-zero crystalline anisotropy numerical evaluation is done to obtain the $f(\tau) \mapsto \alpha$ relation. Here given for 8kG (circles) and 5kG (triangles). Other parameters used: $M_S = 1\text{MA/m}$

lipticity in the polarization of light, one should consider a precession motion taking place in the XZ-plane. Thus the X- and Z-component of magnetization oscillates while the Y-component only increases during the damping of the precession. With the oscillation of the Z-component also the associated demagnetization field oscillates. When the magnetization rotates out of the sample plane the demagnetization field increases and tries to pull the magnetization back to the inplane direction. This changes the total or net applied field in an oscillating manner resulting in a elliptical precession. This only applies in the limit of small precession excitations. For larger excitation the increased angle between net field and magnetization direction when moving out of the plane causes an increasing precession frequency and description is not analytically possible anymore.

Substitution of the physical solution of equation 4.1 in the LLG equation leads to expressions for ω, ϕ, χ and τ:

$$\omega = \frac{\sqrt{4H_0(H_0 + M_sN) - M_s^2N^2\alpha^2}\gamma}{2(1 + \alpha^2)} \tag{4.2}$$

$$\xi = \frac{\sqrt{H_0(H_0 + M_sN)}}{H_0} \tag{4.3}$$

$$\tau = \frac{1 + \alpha^2}{(H_0 + 1/2M_sN)\alpha\gamma} \tag{4.4}$$

$$\phi = \text{ArcSec}[\frac{2}{\sqrt{4 - \frac{M_s^2N^2\alpha^2}{H_0(H_0+M_sN)}}}] \tag{4.5}$$

with H_0 the external field applied in the plane [A/m] and N the demagnetization factor dependent on geometry, usually $N = 1$ for thin films.

In the more complex case of a total field that is neither perpendicular nor inplane the solution to LLG is no longer given by 4.1. The solution is not simply elliptical anymore nor is the damping exactly exponential. Tough the damping can be approximated with an exponential function, the relation between the time constant in this exponent, τ and the Gilbert damping factor α as given in equation 4.4 for the inplane case cannot be obtained analytically.
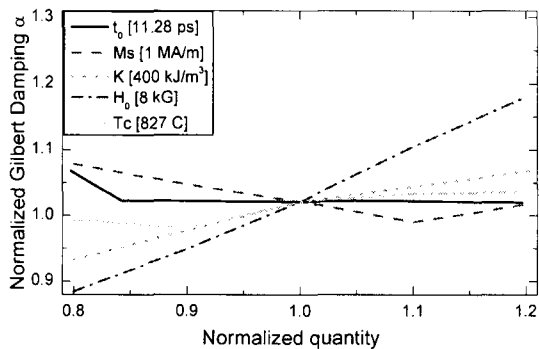
Figure 4.9: The resulting error in the obtained Gilbert damping constant α as function of the error in the assumed input quantities. The assumption for the time constant in the exponential temperature decrease ($t_0 = \delta_0^2/4D$), for the saturation magnetization (M_s), for the anisotropy constant (K), for the applied field (H_0) and for the Curie temperature (T_c). All quantities are normalized with the assumed value and plotted from -20% to $+20\%$.

Therefore numerical evaluation of LLG is performed in Matlab and an approximated relation between timeconstant τ and damping constant α is obtained. In figure 4.8 the numerical solution for $f(\tau) \mapsto \alpha$ for an external field of 5 and 8kG is plotted together with the same relation for the analytical solved case of inplane field. This numerical solution for the relation between τ and α will be used for evaluation of the precession data taken on the HAMR samples.

As an example for the evaluation of the data one measurement is plotted in figure 4.6 (right pane) together with a simulation of the precession in the given configuration and using all media parameters as given in table 4.1 (left pane).

From the measurement the amplitude of precession is calculated by subtracting adjacent maxima and minima. The obtained precession amplitudes are plotted at the average time of the occurrence of the maximum and minimum in an amplitude versus time graph, see the right pane of figure 4.7. Fitting of an exponential function in the amplitude decay-plot of figure 4.7 gives the time constant τ for the particular measurement.

Here it is also done for the simulation, every successive pair of stars in is subtracted and plotted at their average time in figure 4.7 (left pane). This gives a numerical approximate relation between τ (fitting of an exponent in figure 4.7) and α (input parameter for the LLG evaluation).

With this method some errors are made. First of all, as noted before, the damping in this more complex case is not exactly exponential due to the angle between equilibrium magnetization and demagnetization field. Furthermore because the anisotropy constant (K) as well as the saturation magnetization (M_s) decreases with temperature the equilibrium magnetization direction, the precession frequency and amplitude changes with time during the cooling process. Finally, since the amplitude is only measured at the maxima in the precession also an error is made by the simple average method used to obtain a time for every amplitude. This error is clearly visible as alternating points above and below the fitted exponential in both the simulated and measured amplitude graph in figure 4.7. Although it is possible to correct for this error by using an exponential weighted averaging method this is not done because the error made is not adding up systematically and vanishes when enough points are present in the amplitude graph.

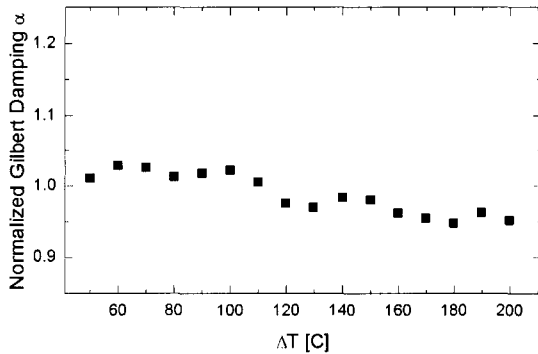For the simulation LLG is evaluated for a quasi static temporal temperature. With tem-

Figure 4.10: Potential temperature dependence of the $f(\tau) \mapsto \alpha$ relation is explored. Here the error in the obtained Gilbert damping α is plotted as function of applied temperature, clearly the error produced is about 4%

perature also M_s and K are changing according to figure 3.5. Dependent on the diffusion rate chosen for the simulated temperature profile versus the diffusion rate in reality an error is made by comparing damping time constants (τ) with simulations to obtain Gilbert damping constants (α). Moreover by using the measured or assumed values for the constants K, M_s, T_c and H_0 in the simulation errors are made when the used values differ in reality. To get an idea of the errors made in this way, simulations are done with $\pm 20\%$ changed parameters. Then using the $f(\tau) \mapsto \alpha$ graph obtained from the simulation with unchanged parameters the Gilbert damping is recalculated. In figure 4.9 the normalized Gilbert damping is plotted against the percentile error in the parameters. Fortunately the error in the Gilbert damping due to a 20% error in one of the parameters is lower than 10%. The highest error is made with the external field , which is measured with an accuracy much higher than 20%

The Gilbert damping dependence on pump power is one of the main goals of this measurement. The obtained Gilbert damping from simulations at different temperatures should therefore be constant (in the simulation Gilbert damping α is assumed to be constant). Otherwise this method to obtain Gilbert damping from the fitting of an exponential curve in the amplitude development is not a valid method, or at least a very suspicious method. In figure 4.10 the normalized Gilbert damping is again plotted, this time against the temperature change. Since in the simulation for every temperature the same Gilbert damping is chosen the obtained value for α should be constant. As can be seen in figure 4.10 this is indeed almost constant (less than 5% change over the full temperature range).

For the field dependent measurements a comparable numerical relation is made as shown in figure 4.8 for the conversion from the obtained amplitude decay time constants (τ) to the Gilbert damping term as it appears in the LLG equation (α). As said before and shown in figure 4.9 a changed applied field has a large influence on the $f(\tau) \mapsto \alpha$ relation, in fact this simple version is not usable because the errors made will be to large. Therefore the numerical relation is extended for varied applied field, adding a third dimension to the graph, which is presented in figure 4.11.

4.2.2 Temperature and Doping dependent Damping

With measuring the precession at different pump powers and calculating the damping constant α through the above mentioned scheme a damping dependence on temperature is found. In figure 4.12 the Gilbert damping parameter is plotted against the pump power. Clearly the Gilbert damping increases linearly with sample temperature for all samples ex-
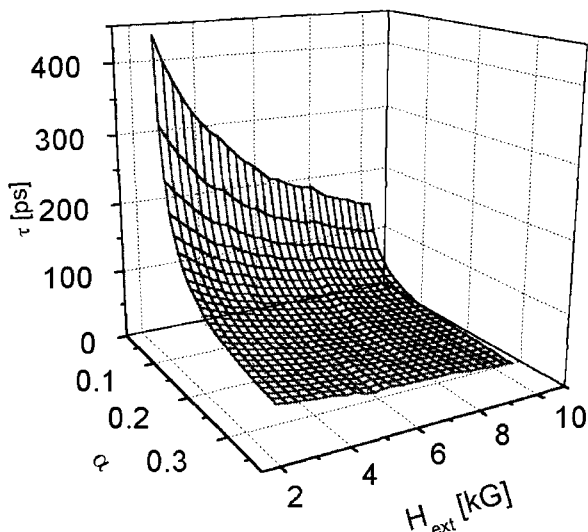
Figure 4.11: Numerical solution of LLG with varied values for α and H_{ext} and fitting of an exponential curve in the amplitude decay gives a relation $f(\tau, H) \mapsto \alpha$, this relation is used for deducing Gilbert damping parameters from field dependent measurements.

cept for sample 11B, the sample with the highest doping level. This can be an intrinsic effect. For example when two damping channels are used, the first channel is dependent on temperature and the second is only dependent on doping level where at higher doping level the contribution of the first channel is not significant anymore. But more plausible is that sample 11B has a complete different structure as also is suggested by the the sample properties and hysteresis presented in the beginning of this chapter.

Except the dependence on pump power also a dependence on doping level is present. In figure 4.13 the Gilbert damping is plotted against the doping level, for the four samples with grain boundary a linear dependence of the damping on the doping applies. The sample without grain boundaries lays a little bit off the straight line. This can be explained as follows. With decreasing doping level the exchange coupling between grains increases proportional, but when the boundary completely vanishes it is replaced by magnetic material and the film discontinuously changes from grain structure to a more or less continuous film. Not really continuous, because the seed layer still exists and forces the film to grow in a grain structure. There is only no material available during the sputtering process to fill the grain boundaries.

The slope in the Gilbert damping versus pump power is plotted against the doping level in figure 4.14. Again sample 11B breaks the rule of proportional dependence, and also the non doped sample lays a little bit off the straight line.

Note that with increasing pump power the Gilbert damping increases and, of course, also the amplitude of precession increases. Possibly it is the precession amplitude causing the higher damping rather than the elevated temperature of the sample. Therefore damping measurements are also done with varying the external applied field, presented in the next section.

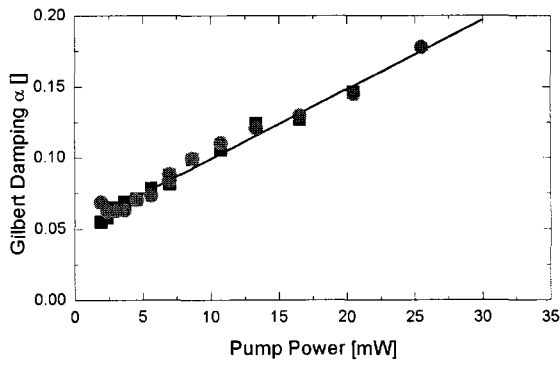### 4.2.3 Field and Doping dependent Damping

Gilbert damping in Perpendicular recording media is measured as function of applied field. Fields are applied 45 degrees to the sample plane as in the pump power dependent measurements and are varied between 0.1 and 1 Tesla. In figure 4.15 the results are plotted for
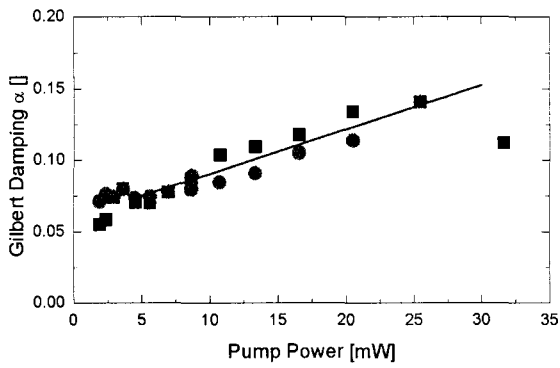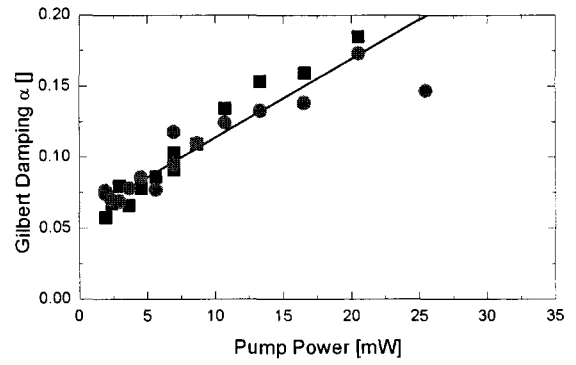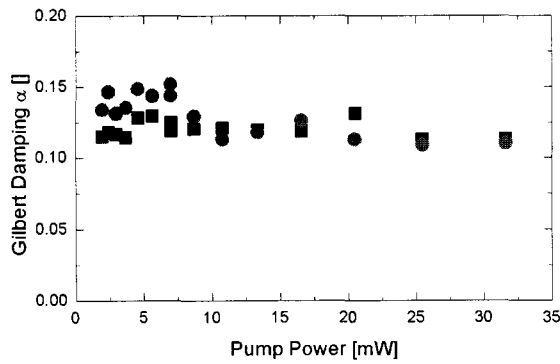
(a) Sample 7B, 0% doping.
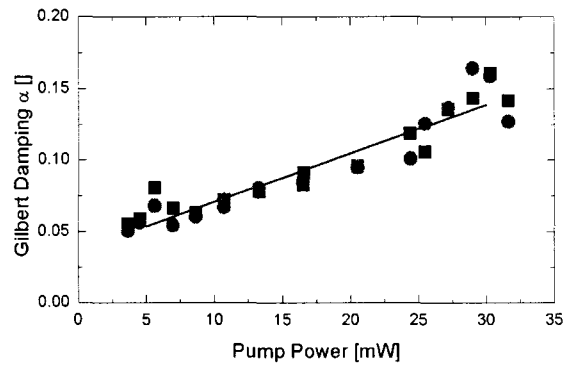
(b) Sample 20B, 0.20% doping.

(c) Sample 17B, 0.35% doping.

(d) Sample 14B, 0.50% doping.

(e) Sample 11B, 0.65% doping.

Figure 4.12: Gilbert damping dependence on pump power for +8kG (squares) and
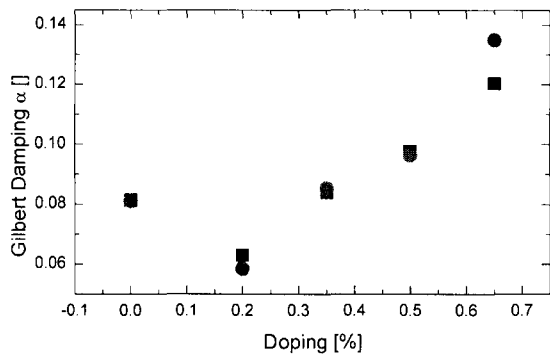−8kG(circles)

Figure 4.13: Gilbert Damping at 7mW pump power versus doping level for +8kG (squares) and −8kG (circles). Except the measurement on the 0% doping sample the points show a clear linear dependence.
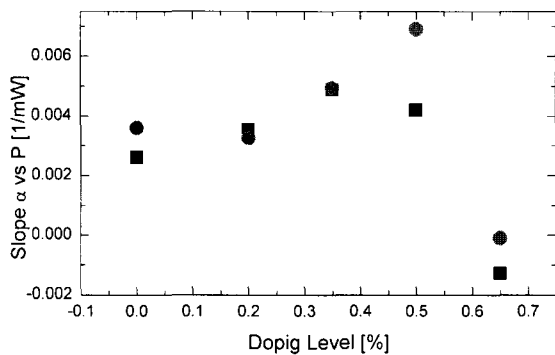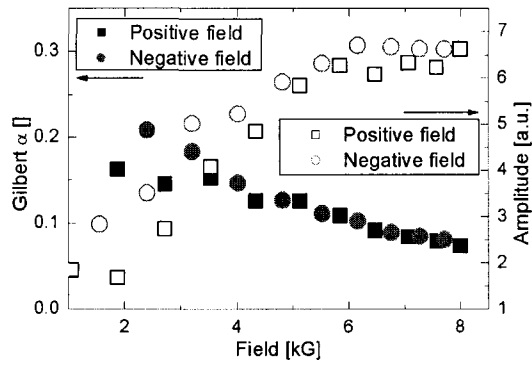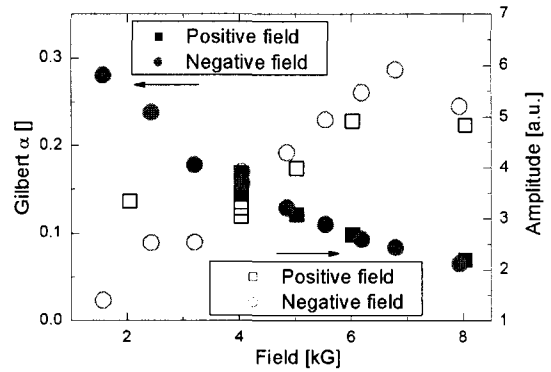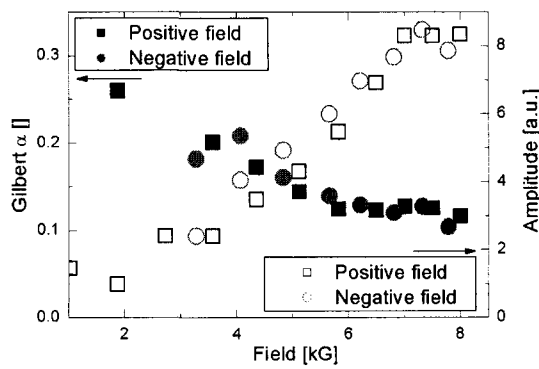

Figure 4.14: Slope in the Gilbert damping vs pump power dependence on doping level +8kG (squares) and −8kG (circles). Except the last measurement, the measurement where there was no clear pump power dependence for α, the dependency of α on pump power shows a dependence on exchange coupling.

(a) Sample S7B, 0% Doping.

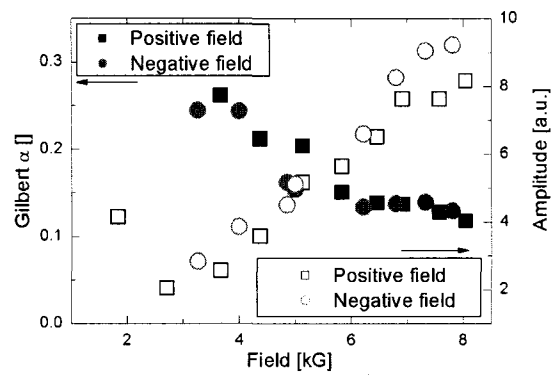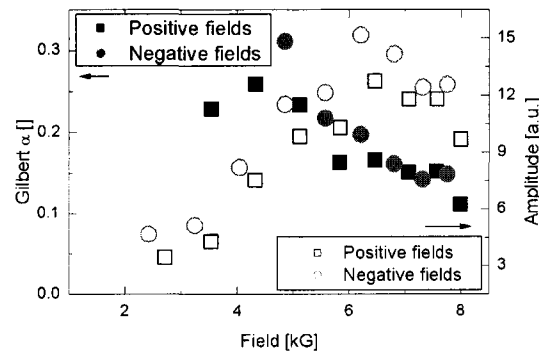(b) Sample S20B, 0.2% Doping.

(c) Sample S17B, 0.35% Doping.

(d) Sample S14B, 0.5% Doping.

(e) Sample S11B, 0.65% Doping.

Figure 4.15: Gilbert damping (closed markers) and precession amplitude (open markers) depending on external applied field, for positive (squares) and negative (circles) fields. All measured with a pump power of 10.7 mW except sample 20B, which is measured with 13.3mW.
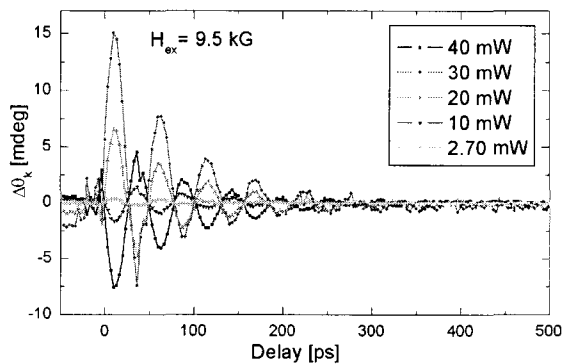
Figure 4.16: Pump dependent precession measurements in a continuous Ni film with an external field applied under 45 degrees with the sample plane. The film has no crystalline anisotropy, the magnetization will lay in the plane due to the shape anisotropy.

the samples with increasing exchange decoupling, all measured using 10.7mW pump power except for sample 20B (figure 4.15(b)) where a pump power of 13.3mW is used. According to the pump power dependent results as presented in figure 4.12(b), the damping in this particular measurement is higher than in the other field dependent measurements.

Clearly the damping decreases for increasing field while the precession amplitude increases for increasing field. The latter, to start with, is easy to understand. The larger the applied field the larger the excitation will be. When the field becomes large compared to the anisotropy field then the equilibrium will also change considerably towards the orientation of the external field making the net excitation and thus precession amplitude smaller again. This can also be seen in the figures 4.15(a) until 4.15(e), first the amplitude increases linearly with field, while it saturates at larger fields closer to the anisotropy field.

Contrary to the pump power dependent measurements the precession decreases with increasing amplitude. Another difference to the pump dependent measurements is the influence of exchange coupling. In the pump dependent measurements there is some exchange coupling dependence in the slope of the pump power dependence. While the field dependent Gilbert damping is similar for all samples including 11B and 7B, the samples with the highest and the lowest doping concentrations.

4.2.4 Comparison with Continuous Ni film

As a reference to the measurements on granular, and thus complicated, PMR media similar measurements are done on simple continuous nickel thin film with inplane magnetization due to shape anisotropy only. In figure 4.16 a selection of precession measurements at different pump powers is presented. These pump powers should not be compared with powers noted in the measurements on PMR media since those are done with a different objective and at a slightly different setup alignment. Nevertheless within this measurement pump powers are comparable.

Using another numerical relation for the Gilbert damping, α versus the exponential decay of precession amplitude, τ, a Gilbert damping versus applied field graph is obtained, figure 4.17. As can be seen in this graph, there is no clear dependence on pump power which is contrary to the measurements done on PMR media.

Figure 4.18 shows a selection of the field dependent measurements on a nickel film. Computation of those precession graphs towards a Gilbert damping, again using a numerical relation $f(\tau) \mapsto \alpha$, leads to figure 4.19. Here clearly there does exist a fairly strong depen-
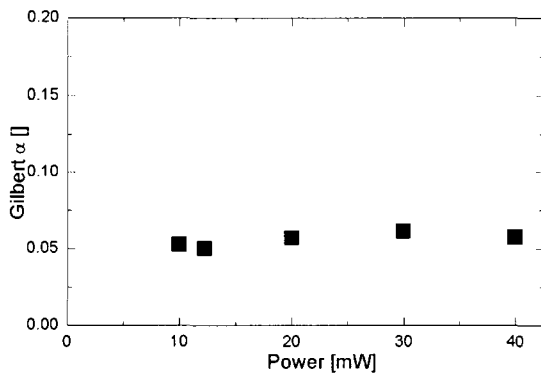
Figure 4.17: Gilbert damping depending on pump power in thin Nickel film. There is no clear dependence, the increase of the damping is less than 20% when the power is 4 times increased.
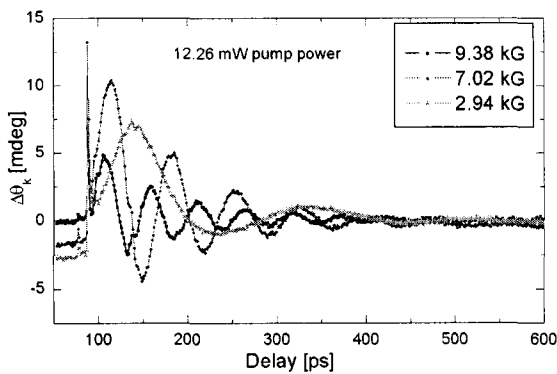
Figure 4.18: A selection of the field dependent precession measurements on thin nickel film.
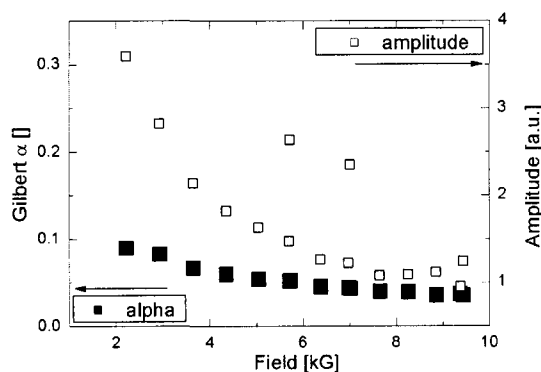
Figure 4.19: Field dependent measurement of the Gilbert damping and the amplitude of precession in a thin nickelfilm as deduced from the measurements presented in figure 4.18. Clearly damping as well as the amplitude decrease with increasing field. Nice also is that at the two points around 7kG where the amplitude is a bit off from the main stream the damping parameter is still in the mainstream, which again shows that the method for deducing α from τ is not sensitive to the amplitude of precession.

Table 4.2: Summary of Gilbert damping dependencies on Nickel film and perpendicular recording media (PMR). + means positive proportional, − means negative proportional and 0 means no dependency.

	Pump Power	Applied Field
PMR, Gilbert damping α	+	−
PMR, Precession amplitude	+	+
Ni, Gilbert damping α	0	−
Ni, Precession amplitude		−

dency of damping on applied field.

Two points in the amplitude graph of figure 4.19 are not in the straight line. This can be due to a misalignment, for example when the reflected beam is not completely collected on the diodes, resulting in the same behavior but with lower signals. This nicely shows that the method for deducing Gilbert damping parameter α from the exponential decay of amplitude is not sensitive to the height of the measured signal. Note that the damping still might depend on precession amplitude.

4.3 Conclusions and Recommendations

Most striking result is that the Gilbert damping in perpendicular recording media (PMR) increases with pump power (and precession amplitude), while the damping does not change in continuous a Ni film. Gilbert damping decreases with increasing applied field (and precession amplitude), as also observed in the Ni film and similar as earlier observed by Wu et al. [18] in permalloy. In table 4.2 an overview is given of all the proportionalities and comparison with nickel thin film is made.

Further, the Gilbert damping clearly increases with doping level and thus with exchange decoupling. Also the slope in the pump power dependence of the PMR samples has a slight dependence on doping level. Here an exception is found for the sample with zero doping and the one with maximum doping (0.65%). In the case of zero doping the grain boundaries are replaced by magnetic material, causing a discontinuous transition from the sample with 0% doping to samples with some doping. At the highest doping level a measurement problem arises making it impossible to measure the Gilbert damping depending on pump power.

The exchange decoupling dependence of the Gilbert damping can be due to the fact that with the pump probe technique many grains are measured and averaged. With higher decoupling the change for dephasing of the isospin increases. Although special care is taken to pump the complete probed area to a constant temperature, there always exists a radial temperature gradient in the pump spot and thus in the probed area. Also anisotropy, shape and size distributions of the grains over the probed area may give rise to precession dephasing. As a last contribution also the magnetic field from a neighboring grain will add up to the local field making the local field non-constant which might work constructive or destructive for the precession but certainly destructive in average.

An other effect which might be responsible for the enhanced Gilbert damping in the high doped recording media is the spin pumping effect as predicted by Tserkovnyak [16].

The field dependence of the Gilbert damping cannot only be explained with a grain effect since it is also observed in the nickel film and in permalloy. A possible explanation is the direction with respect to the anisotropy axis. With increasing field the equilibrium magnetization will be pulled out of the anisotropy direction. This suggests that the Gilbert

damping is anisotropic in al three materials.

Qiang Zhang [20] also reported an anisotropy in the intrinsic Gilbert damping in ferromagnetic CrO_2 thin films. But they observed an increase in damping rate when the external field direction moves towards the hard axis. Thus in the case of thin Ni films and an applied field under 45 degrees this would result in an increase of damping rate with field rather than a decrease. Platow et al. [21] reported a similar angle dependence of the FMR linewidth of Ni films. Platow also showed a temperature dependence of the FMR peakwidth, where the width increases proportional with the temperature. Platow suggests that magnetocrystalline effect might be the underlaying mechanism but further studies need to be done.

More measurements should be done on simple thin nickel films to separate grain effects on the damping from more intrinsic effects. Field angle dependent damping measurements might illuminate the strong field dependence of the damping obtained in the nickel film. To certify a complete absence of power dependence of the Gilbert damping in nickel more and more accurate pump power dependent damping measurements on nickel film should be done. And more direct temperature dependent damping measurements can be obtained with an bias sample temperature applied with an heating stage.
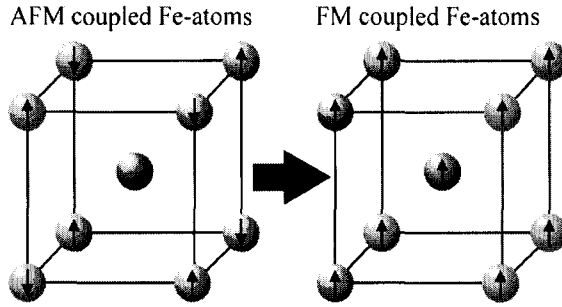
Figure 5.1: FeRh naturally has the bcc structure. Iron in FeRh is antiferromagnetic coupled mediated by the rhodium atom. At elevated temperatures the antiferromagnetic coupling changes to ferromagnetic due to thermal fluctuations in the electronic structure of the rhodium atom.

5 Ultrafast Ferromagnetic Ordering in FeRh

Besides magnetic recording media other material of interest for study of the ultrafast magnetization dynamics is Iron-Rhodium (FeRh). Iron-Rhodium alloy in the bcc structure is known since its discovery by Fallot in 1938 to have a metamagnetic phase transition from antiferromagnetic (AFM) to ferromagnetic (FM) at a temperature of approximately 360K [22], see figure 5.1. Thiele et al. [8] recently showed that a bilayer of FePt/FeRh can form an exchange-spring system. FePt has high anisotropy and high coercivity while FeRh is antiferromagnetic at room temperature but upon heating above the transition temperature becomes ferromagnetic with a large magneticmoment and low anisotropy. When the bilayer is heated above the transition temperature the inplane magnetic moment of FeRh helps the external field to switch the "hard" FePt layer. This opens intriguing possibilities for Heat Assisted Magnetic Recording media (HAMR), where the ferromagnetic FeRh assists the heated media to switch while the antiferromagnetic FeRh at room temperature supports the long-time stability. For use in magnetic recording media the time necessary for the FeRh to change its phase from AFM to FM is of crucial importance since I) this gives a limit to the data write speed and II) long term heating of a particular bit also increases the temperature of surrounding grains imposing a smaller data density.

Insight in the temporal behavior during the phase change of FeRh is also of scientific importance since the exact process is still a matter of debate. Kittel originally proposed a model based on lattice expansion driven exchange inversion [23]. While Gruner et al. [22] proposed a rhodium moment fluctuation mechanism as a base for the phase transition. Further is the gain of ferromagnetism, as an inverse of magnetization quenching when heating above Curie temperatures, an interesting facet in the debate about the origin of ultrafast laser-induced change of magnetization of ferromagnetic materials.

Here for the first time experimental evidence [24] is presented that ferromagnetic ordering in FeRh can be induced on the picosecond timescale (!) when heated with optical pump pulses of femtosecond duration. Such an ultrafast generation of ferromagnetic ordering opens up unprecedented novel options for heat assisted magnetic recording schemes. Apart from demonstrating the ultrafast timescale for the phenomenon of ferromagnetic ordering
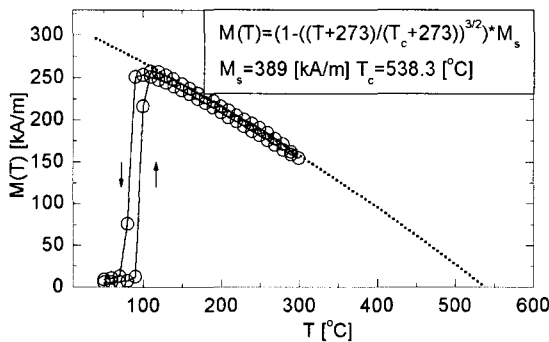
Figure 5.2: Magnetic moment versus temperature measurement of FeRh together with a fit to obtain T_C

an analysis is presented that leads to a more detailed interpretation of the magnetization dynamics after the ferromagnetic phase set in.

In the next section first the sample preparation is described together with a brief recapitulation of the pump-probe setup as used for the measurements of the magnetization dynamics on FeRh. In section 5.2 the results demonstrating the ultrafast nature of the metamagnetic phase change are presented. Following in section 5.3 is a description given of the proposed model that describes the observed magnetization dynamics after the first initiation of a ferromagnetic phase. In section 5.3.2 this proposed model is compared with the measurements. Finally in section 5.4 the conclusions on the measurements presented here are given and recommendations for future measurements of magnetization dynamics in FeRh are given.

5.1 Experimental Setup

The investigated FeRh sample is a 100nm thick $Fe_{45}Rh_{55}$ film deposited on a MgO single crystal substrate. Deposition is done using magnetron sputtering followed by a thermal annealing at 975K. In figure 5.2 the temperature dependence of the magnetization is given. As can be seen in this figure there is a temperature hysteresis in the magnetization. The hysteresis is probably caused by a stabilizing effect of the ferromagnetic phase due to the lower energy of aligned spins.

With the pump-probe setup as described in chapter 3 magnetization dynamics are measured in this FeRh sample. A pump pulse heats a small spot on the FeRh thin film, a second time delayed probe pulse then measures the reflectivity and the Kerr rotation. With mechanically modulating the pump beam the transient effects are obtained. i.e. Kerr rotation and reflectivity are measured with and without the pump pulse, with the lock-in detection scheme both measurements are subtracted and only the pump induced transient Kerr rotation and reflectivity are recorded. In this setup only the Kerr rotation due to the polar Kerr effect is measured. Therefore the transient Kerr measurement directly reflects the transient, or pump-induced, dynamics in the polar component of the magnetization:

$$\Delta \Theta_k(t) \propto \Delta M_z(t), \qquad (5.1)$$

with $\Delta \Theta_k$ the transient Kerr effect and M_z the z-component of the magnetization.

Reflectivity measurements represents the electronic temperature, reflectivity increases linearly with the temperature of the electronic system. For FeRh there is an additional contribution to the transient reflectivity. When the electronic structure changes from antiferro-

magnetic to ferromagnetic it is accompanied by a change in the reflectivity:

$$\Delta R = a \cdot \Delta T(t) + b \cdot \Delta |\mathbf{M}(t)|, \tag{5.2}$$

with a and b proportionality constants, Δ stands for "pump induced", R the reflectivity, $T(t)$ the contribution to the reflectivity linear dependent with the temperature, and $|\mathbf{M}(t)|$ the length of the magnetization vector. The temperature contribution to the transient reflectivity consists of a contribution due to the electronic temperature and a contribution due to the lattice parameter. Besides the time needed to heat the phonons by electron-phonon scattering as described in the 3T model the lattice also needs time to expand before it contributes to the reflectivity. Lattice expansion goes with the speed of sound, expansion of the lattice throughout the whole probed area on the sample typically takes a few picoseconds. The length of the magnetization is an average over the probed area of the absolute value of the magnetization. It is still possible to have no net magnetization in the total probed sample area while it is in the FM phase. The probed area than contains a number of magnetic domains who are not aligned or even opposite oriented. The measurement of $|\mathbf{M}(t)|$ is a nice measure of achieved phase transition because purely the forming of a magnetization is measured rather than the process of aligning of different domains throughout the sample. The Kerr measurement measures the net magnetization of the sample.

Since FeRh changes from antiferromagnetic to ferromagnetic a transient Kerr effect will only be observed when the pump power is high enough to reach the transition temperature. When the temperature reaches the Curie temperature at really high pump powers the magnetization in the just formed ferromagnetic phase will be quenched again. In the next section the results in the transient Kerr effect at low and at high pump power is presented. Form the results it can be concluded that at low power the temperature is to low to reach the transition temperature in FeRh. At high pump power the transition is easily reached and the time necessary to fully develop a magnetic moment is the time necessary for the phase transition.

5.2 Results ultrafast Ferromagnetic Ordering

The time evolution of magnetization after excitation with a pump pulse is shown by the Kerr rotation in the left pane of figure 5.3. For this graph the difference in transient Kerr response at positive and negative applied field is presented to avoid crosstalk between polarization and reflectivity. A trashhold behavior can clearly be seen, at low pump power no Kerr activity is seen while at slightly larger pump power clear transient Kerr rotation appears. With increasing pump power the transient Kerr peak keeps increasing due to an increasing part of the probed volume which reaches the transition temperature for a period long enough to change its phase. In the right pane of figure 5.3 the simultaneous recorded reflectivity is shown. Even for the lowest pump powers there is a clear transient reflectivity. With increasing pump power the reflectivity increases, it increases linear due to the increase in temperature and its shape changes slightly due to a increase in the contribution of the ferromagnetic electron structure, according to equation 5.2.

To obtain the contribution of the length of the magnetization in the ferromagnetic phase to the transient reflectivity the difference is taken between the transient reflectivity above and below the transition temperature. In the left pane of figure 5.4 the first 100ps of the transient reflectivity is shown. The transient reflectivity curve for a temperature above and below the transition temperature of the magnetic phase transformation are normalized to 1. For the transient reflectivity in the AFM phase a spline-fitting is taken because no measurements were done at the same high resolution as for the transient reflectivity in the
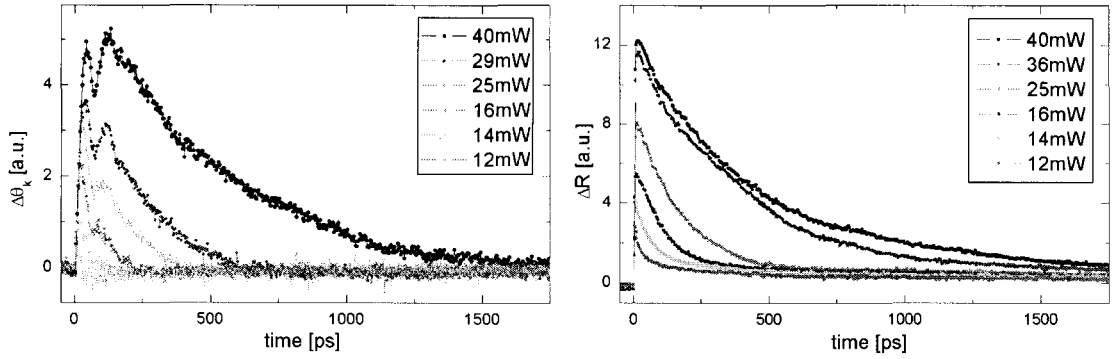
Figure 5.3: Left: Kerr rotation for increasing pump powers. At low power (12mW) no peak is observed while at higher powers a sudden Kerr peak appears. At low powers the temperature is not high enough to change the magnetic phase of FeRh. At higher the transition temperature is reached. At increasing pump power the continues increase in Kerr rotation is due to the increasing thickness of FeRh film reaching the transition temperature long enough to change its phase to the ferromagnetic ordering. Right: The reflectivity recorded simultaneously with the Kerr rotation. Even at the lowest powers a clear change in reflectivity is seen.
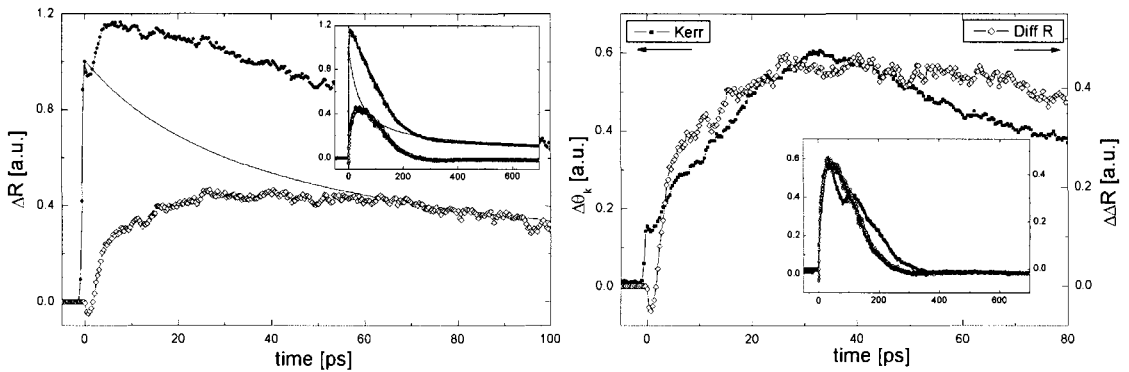
Figure 5.4: Left: Normalized reflectivity at a pump power below (line) and above (circles) the transition temperature and the difference of the two reflectivities (open diamonds) representing the phase transition accompanying electronic structure change and lattice expansion. The transient reflectivity below the transition temperature (the line) is a spline-fit in a lower resolution measurement. Right: The reflectivity change due to the AFM/FM phase chance (open diamonds) compared with the Kerr rotation representing the normal component of the net magnetization. The initial negative dip in the diamonds curve is due to the lack of resolution in the subtracted AFM reflectivity curve.

Figure 5.5: Three proposed mechanisms producing the doublepeak behavior explained in a M(T) graph. a) Large heat flux between the subsystems of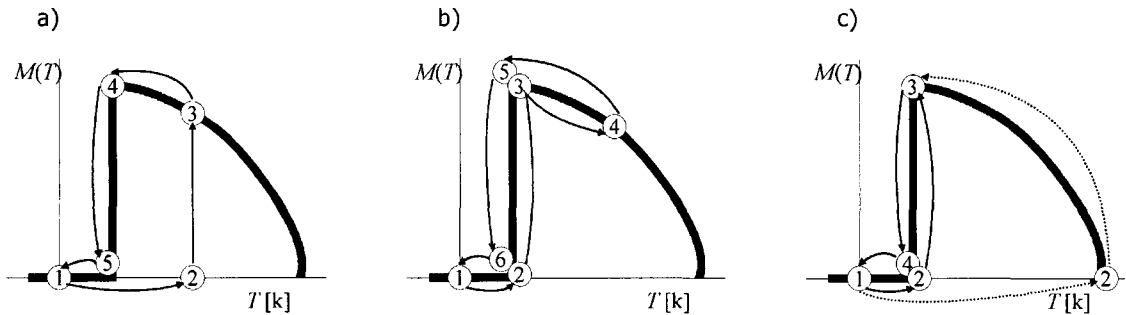 the 3T model are assumed, double peak is caused by precessions initiated by the fast production of magnetic moment. b) Slow heat transport between the spin system and the other systems causes the spins to slowly follow the the instantaneously applied temperature. The spin system temperature will go through all temperatures when heating up. c) The sample thickness is the basic cause of the double peak. deeper parts of the sample are heated to another temperature than surface parts. Together with the nonlinearity of the T dependence of M results in a double peak.

FM phase. Substraction of the two normalized transient reflectivities in the FM and the AFM phase gives the contribution of the length of the magnetization:

$$\Delta_p \Delta R \propto \Delta |\mathbf{M}(t)|, \tag{5.3}$$

where Δ_p means the normalized difference above and below the AFM/FM transition and Δ means the pump induced difference. In the right pane of figure 5.4 a comparison is made between the absolute magnetization ($|\mathbf{M}(t)|$), measured through the reflectivity, and the net magnetization in the z-direction ($M_Z(t)$), measured through the Kerr effect. The reflectivity curve in the AFM phase was measured with a resolution of 3ps while the reflectivity in the FM phase is measured with a temporal resolution of 0.3ps. This difference in temporal resolution between the two subtracted reflectivity curves is the cause of the negative dip at $t = 0$ps.

Clearly visible in figure 5.4 is the ultrafast generation of ferromagnetic ordering! Magnetic moments are fully developed within 20ps and after 30ps a total net magnetization in the z-direction is in its maximum. Moreover in the net magnetization a second local maximum can be seen at approximately 150ps, The nature of this second peek will be analyzed in the next section. Further measurements of the transient Kerr effect will be presented and compared to simulations of a proposed model.

5.3 Simulation of Magnetization Dynamics

As remarked in the previous section there is a second local maximum at approximately $t = 150$ps in the Kerr effect and thus in the z-component of the magnetization. In this section three models are proposed who are able to describe the doublepeak behavior. Then with further analysis two proposals are rejected and the third is worked out in more detail and compared with the measurement data.

In figure 5.5 the three proposed models are schematically presented. In a) The heat transport between the electronic system and the spin system is assumed to be much faster than the time needed for macroscopic diffusion. b) Assumes a heat transport from the electronic

system to the spin system of comparable speed to the macroscopic diffusive transport. For c) the thickness of the sample is taken into account. The surface part here is assumed to be hotter than deeper parts of the sample. First the deeper parts produce a magnetic moment while the top part is so hot that it is even beyond the Curie temperature. After some diffusive cooling the deeper parts are back to the AFM phase while the top part cools through the FM phase again.

To study the above mentioned mechanisms in more detail some additional concept will be introduced to better quantify the different heat transport mechanisms and time constants. Thereafter the three proposals will be discussed again but in more detail followed by an argumentation why only proposal a is able to describe the observed magnetic behavior.

According to the 3T model a spin temperature can be defined as the temperature connected to the magnetic moment as defined by $M(T)$ in figure 5.2. Thus $M = M(T_s)$ and in thermal equilibrium $T = T_s$ and thus $M(T) = M(T_s)$ applies. Equilibration of temperature between the three subsystems depends on heat transfer between them and therefore will take some time. For the sake of simplicity the heat flux is assumed to be linear with the temperature difference between the electronic and the spin system. The spin temperature therefore will increase until it reaches equilibrium with the electron temperature:

$$\dot{T}_s = \frac{T_e - T_s}{\tau_s}, \tag{5.4}$$

with τ_s a specific time constant and T_e the objected final temperature of the spin system. With this equation the heat transport from the electronic system through the phonons to the spin system is neglected. An eventual contribution of this mechanism will be collected in the time constant τ_s.

Even if the sample is completely in the ferromagnetic state it still can be non-magnetized, the separated magnetic domains are not aligned and cancel each other. The growing of a total net magnetization, the aligning of individual spins, is a complex process. One can imagine one or multiple nucleation sites from where the magnetization laterally grows, or a more uniform aligning process where all spins are individually precessing in each others exchange field. But as a first order approximation the speed of aligning of individual spins to a net magnetization is linear proportional to the magnetic moment of the individual spins. Thus for the magnetization an exponential growth is assumed:

$$\dot{M} = \frac{\mu(T_s) - M}{\tau_m}, \tag{5.5}$$

with $\mu(T_s)$ the maximum magnetization at the actual temperature according to figure 5.2, τ_m a specific time constant and M the net magnetization.

Following the three mechanisms potentially responsible for the double peak behavior in the transient Kerr effect will be described again but in more detail.

In figure 5.5 c) the thickness of the sample is the real cause of the double peak. The top part of the sample follows the dotted line while a deeper part of the sample follows the straight line. The sample surface is heated beyond the Curie temperature, therefore is not in the FM phase (1 → 2, dotted line). The temperature is so high that the magnetization is quenched again. The pump beam penetrates the sample with a finite distance while the pump energy decreases exponentially with the distance. Therefore there must be a depth into the sample where it is just heated enough to reach the ferromagnetic phase (1 → 2, straight line). This deeper part of the sample causes the first peak in the transient Kerr measurement. Now during cooling the deepest parts of the sample will cool through the transition temperature and become antiferromagnetic (3 → 4, straight line). This causes a

decrease in magnetic signal. Meanwhile the top layer is also cooled by macroscopic diffusion and cools back through the Curie point. With the cooling of the top layer towards the transition temperature ($2 \rightarrow 3$, dotted line) another magnetization peak appears[1]. The non-linearity of the M dependence on T is the basic cause for a double peak behavior where the circumstances are changed gradually.

If one assumes the time constant τ_s for the heat transfer between the electronic system and the spin system to be large, cf. diagram b), another cause for the double peak is obtained. The electrons are heated instantaneously to a high temperature, higher than 4 in diagram b). The spin system follows slowly and thereby goes through the maximum in the $M(T)$ graph (3). This causes the first peak. Before the electrons are cooled back through the transition temperature the spins reach an even higher temperature (4). Then the electrons are further cooled by macroscopic diffusion, the spins will follow again by reversed heat transport between the two systems. The spin system cools back through the maximum in the $M(T)$ graph ($4 \rightarrow 5$) causing the second peak.

In case a) of diagram 5.5 there is no double peak behavior. Here the heat flux between the electronic and the spin system is assumed to be very large, the spins will react instantaneously on the pump pulse ($\tau_s = 0$). The real cause of the double peak now lays in the fact that the Kerr effect does not necessarily probe the magnetization, but may also reflect orientation dynamics. The initial onset of a ferromagnetic state will be in the direction of the external applied field. Since the phase change is rather fast ($\simeq 30$ps) the phase change will complete to the ferromagnetic state in the direction of the external field. When there is a finite magnetization the direction of the external applied field is no longer the equilibrium magnetization direction. The equilibrium now lays in the direction of the total effective field ($\mathbf{H}_{\text{ext}} + \mathbf{H}_{\text{demag}}$). Since the the phase change is fast it changes before a recessional motion according to LLG is able to reorient the magnetization into the direction of the equilibrium magnetization. The typical time constant of this precessional motion is ($\gamma_0 \mathbf{MH} \simeq 100$ps). Due to a large damping coefficient, either intrinsic Gilbert damping or apparent damping, only two peaks of the precession are seen.

With a more detailed analysis the first two proposals are rejected. The third proposal, the precessional nature of the doublepeak behavior, is made plausible with simulations in the next section who are in high qualitative accordance with the measurements.

The thickness of the sample, as proposed in c) of 5.5 cannot be the real cause of the double peak behavior. Simulations showed that the heat diffusion in the depth of the sample is to small with the given diffusivity and probe penetration to causes a double peak.

The second proposal, where the weak thermal coupling of the electronic system to the spin system leads to a slow heating and cooling of the spin system through the complete M(T) graph, is not a satisfactory description of the observed double peak. The fact that the second peak is not as high as the first peak, as expected with this model, is not the weakest point. The difference in peakheight can be due to diffusion and unequal heating of different parts of the probed area. But the more fundamental problem of this model is that at increasing heating levels (higher pump powers) the second peak should be delayed increasingly, which is contrary to the measurements. The second peak always appears after the same delay, and thus the thermal delay caused by heat transfer between different subsystems can not be the cause of the observed double peak feature.

The third proposal, the precessional nature of the double peak, turned out to well describe the measurements and therefore must be the explanation as the comparison in the following section convincingly shows.

---

[1]The thickness cause for the double peak can also be seen differently: Due to diffusion deeper layers in the sample are heated by the cooling process of top layers.
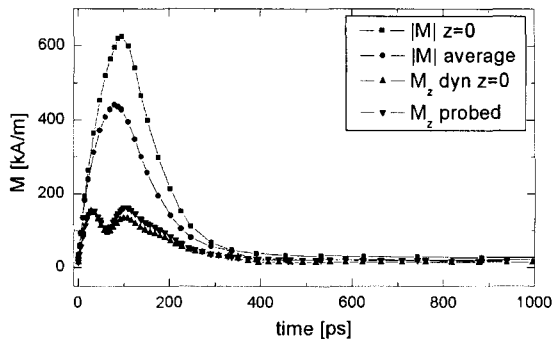
Figure 5.6: Magnetization magnitude at the surface of the sample ($|M|_{z=0}$), average moment in the total ferromagnetic layer ($|M|$ average), the z-direction of M at the surface (M_z dynamic $z = 0$) and the magnetization that would be observed when probing with a depth dependent probe intensity (M_z probed). Used parameters: $\tau_m = 50$ps, $\tau_s = 0$, $T_0 = 33°$C, $\Delta T = 167°$C, $\delta_{0,Red} = 30$nm, $\delta_{0,Blue} = 21.2$nm, $D = 1.994 \cdot 10^{-5}$m^2/s, $M_{s,max} = 760$kA/m, $\alpha = 0.3$, $\gamma_0 = 221 \cdot 10^3$mA/s and $H_{ext} = 3.5$kG$\cdot(e_x, -e_z)/\sqrt{2}$.

5.3.1 Model

Here a model and simulations are described which are able to satisfactory describe the measurements. Basic idea for this model is the assumption that, during the phase change from AFM to FM, the magnetization will initially grow in the direction of the external field and that the time constant for growing a net magnetization (τ_m) is smaller than the time LLG needs ($\gamma_0\mathbf{M}\mathbf{H}$) to rotate the magnetization to a new equilibrium with the demagnetizing field. With this assumption there will be a large initial peek in M_z before a simple precession starts. If now also a large Gilbert damping is assumed (because of either decoherence or intrinsic damping) a double peek like behavior is obtained.

The pump pulse heats the system, depending on the temperature a phase change from AFM to FM will occur where the amount of magnetic moment again depends on the temperature according to figure 5.2. In the temperature dependence of M also some hysteresis is seen. It is not possible to take this hysteresis in accordance for the numerical simulation without making complete micromagnetic calculations. Therefore only the cooling part of the M(T) curve is taken for the calculations. This is probably closest to reality since most parts of the sample cools due to diffusion while only minor parts deeper in the sample are heating up due to diffusion.

To see what the qualitative effects of the different steps in the calculations are, the individual steps are presented here. Using the diffusion equation (3.11) a temperature for every time t and sample layer z is calculated. With the measured data from figure 5.2 a magnetic moment is calculated for each temperature. For the dynamic calculations with LLG an average magnetization over the sample thickness is used, averaging is done over the ferromagnetic part of the sample only:

$$|\mathbf{M}_{avg}| = \frac{\int_0^{L_{FM}} |\mathbf{M}(z,t)|dz}{L_{FM}}, \tag{5.6}$$

with L_{FM} the depth where the sample is just heated enough to be in the FM-phase. In figure 5.7 the thickness of the layer in the ferromagnetic phase is plotted as function of the time. Furthermore for the demagnetization field $\mathbf{H}_{demag} = (0, 0, -\mathbf{M}_{z,avg})$ is used. With LLG and assuming a quasi static magnetization magnitude the dynamics are calculated and
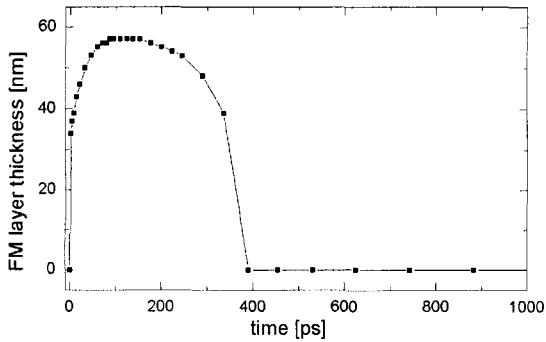
Figure 5.7: The thickness of the ferromagnetic layer as used in equation 5.6, this is the depth into the sample where there is just enough temperature to be in the FM-phase.
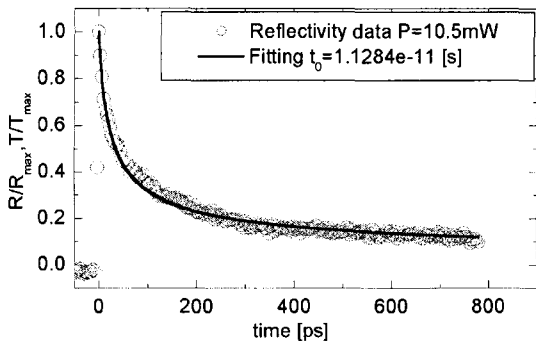

Figure 5.8: Fitting of the reflectivity data at low pump power ($P = 10.5$mW) assuming a Gaussian initial profile and surface probing.

plotted in figure 5.6.

In case of a conducting sample the penetration of blue probe light will be smaller than the penetration of red (pump) light:

$$\delta_{0,blue} = \delta_{0,red} * \sqrt{\lambda_{blue}/\lambda_{red}}, \tag{5.7}$$

with λ the wave length of the light and δ_0 the penetration depth of red (pump) light. The sensitivity of the measurement is proportional to the light intensity of the probe, thus the measured value for the magnetization is a weighted average:

$$M_p = \frac{\int_0^\infty e^{-\frac{z}{\delta_{0,blue}}} \cdot M_z(z,t)dz}{\int_0^\infty e^{-\frac{z}{\delta_{0,blue}}}}, \tag{5.8}$$

with M_p the observed magnetization in the z direction which is proportional to the polar Kerr effect, $M_p \propto \theta_k$. In figure 5.6 all the stages of simulation are plotted for some typical values of the parameters. For averaging, the magnetic moment of the part of the sample that is in the ferromagnetic phase has to be calculated. Assumed here is that there is only one border between FM and AFM phases, such that the FM phase is always on top of the AFM phase. Thus, although in principle possible, it is excluded that the top is AFM and a middle layer FM. Figure 5.7 displays the evolution of the thickness of the ferromagnetic layer for typical values of the parameters. Reflectivity changes linearly with the temperature. However, for
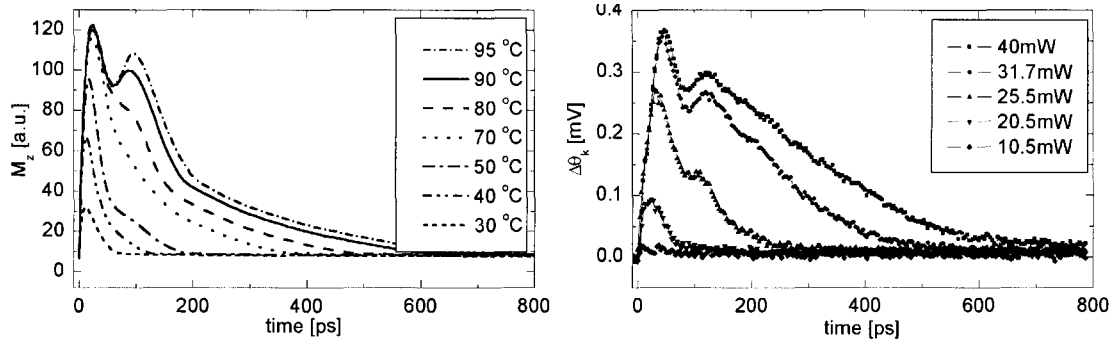
Figure 5.9: Left panel simulations, Used parameters: $\tau_m = 10$ps, $\tau_s = 0$, $T_0 = 58°$C, $\delta_{0,Red} = 30$nm, $\delta_{0,Blue} = 21.2$nm, $D = 1.994 \cdot 10^{-5}\text{m}^2/\text{s}$, $M_{s,max} = 253$kA/m, $\alpha = 0.3$, $\gamma_0 = 221 \cdot 10^3 \cdot$m/As and $H_{ext} = 3.5$kG$\cdot(e_x, e_z)/\sqrt{2}$. Right panel Kerr measurement at five different pump powers.

FeRh there is an additional contribution to the reflectivity due to the phase change. For pump powers too low to reach the transition temperature, the change in reflectivity is linear to only the lattice temperature. Fitting of equation 3.11 in the reflectivity data gives a value for t_0, the diffusion constant D and the penetration depth δ_0 are correlated to each other through $t_0 = \delta_0^2/4D$. Therefore fitting of the data only gives a value for t_0. Fitting is done using:

$$\sqrt{\frac{t_0}{t + t_0}}. \tag{5.9}$$

Refer to figure 5.8 for the reflectivity data together with the temperature fitting. Since the 100nm film looks metallic by eye and the 30nm film is a little transparent the penetration depth is assumed to be approximately 30nm. With this penetration depth the obtained diffusion constant is $0.2 \cdot 10^{-4}[m^2/s]$, literature values for metals are approximately $1.5 \cdot 10^{-4}[m^2/s]$.

In the next section all parts of this simulation model for the magnetization dynamics in FeRh are brought together. Complete simulations are made of the magnetization dynamics as would be observed with the Kerr effect in the polar configuration. For typical values of the parameters, simulation are compared with measured data.

5.3.2 Comparison with Measurements

In this section simulations will be qualitatively compared with obtained pump-probe measurements on FeRh. For the simulation all parts of the model as described in the previous section are combined. i.e. for the simulation the following assumptions are a part of the used model:

- The temperature as given by equation 3.11 with the diffusion constant as obtain with the fit in figure 5.8;

- The dependence of the magnetic moment on the temperature as given by the measured data in Figure 5.2;

- The delay in spin-temperature rise and moment aligning as given in equations 5.4 and 5.5;

- The dynamic response of a magnetic moment in a field as given by the LLG (equation 3.15);

- The averaging over depth as obtained with a probing beam according to equation 5.8.

Using these assumptions a simulation of the measurement is made. In figure 5.9 measurement data (right panel) and the simulation (left panel) are displayed together.

Because the heat diffuses very fast away from the sample, after 270ps is the temperature already 20% lower, either T_0 or ΔT has to be rather large to get the measured long lasting, approximately 500ps, magnetic moment. With increasing ΔT the second peak will also increase and finally surpass the first peak, which is not in accordance with the measurement. This second peak becomes larger than the first peak when the temperature at the time of the first peak is so high that the magnetization is quenched according to figure 5.2. Then, during the cooling process magnetization increases again to reach a maximum at the transition temperature.

Thus the assumptions on temperature and diffusion constant affect the height ratio between the first and the second peak. Practically it turned out that assuming a maximum ΔT for the simulation of the measurement presented in the right pane of figure 5.9 of $95°C$ gives the best correspondence in terms of peak height ratio between measurement and simulation.

The only way to get the magnetic moment in the simulation as long lasting as in the measurement is to assume a large initial temperature. It is plausible that the pump pulses causes an average heating of the sample, i.e. the temperature diffuses away from the metallic layer at the position of deposition but does not completely diffuse away from the sample. The total sample temperature gets elevated after a large number of pump pulses until the average heating of the sample is in equilibrium with its dissipation to the environment.

Since the repetition rate of pump pulses is rather large, 8MHz, this new equilibrium can be reached in a matter of seconds (well before the actual measurement is started). This is supported by the fact that at lower repetition rates we were not able to get any magnetic measurements, the average temperature is considerably lower and the temperature will only be high enough for a very short time.

For the measurements in figure 5.9 an average- or initial-temperature of $58°C$ gave the best results. With this background temperature the magnetic moment in the simulation lasts as long as in the measurement. The difference in steepness of the decreasing part of the graphs can be explained by the lateral distribution of pump and probe. Moreover due to the same stabilizing effect causing the temperature hysteresis in the $M(T)$ graph a lateral stabilizing effect might cause a less steep decrease of the magnetic moment. A lateral stabilizing effect may be expected from lateral neighboring parts below and above the transition temperature. It might be energetically favored to keep small sample parts in the FM phase, even if their temperature is below the transition temperature, when surrounding parts are also in the FM phase. The kink in the high temperature graphs of the simulation is caused by the used $M(T)$ data.

With fitting of the diffusion equation into the reflectivity measurement as done in figure 5.8 only $t_0 = \delta_0/4D$ is obtained, thus either D or δ_0 has to be assumed or obtained differently. Fortunately changing δ_0 and D while keeping t_0 constant does not change the simulation results too much because a smaller diffusion constant D causes an accordingly smaller penetration depth of the pump meaning a larger gradient in temperature, both effects cancel each other more or less for small changes.

The first peak is simply the growth of magnetic moment, the phase change from AFM to FM. The time needed to rise this first peak depends on the timeconstant τ_m. The second peak is a dynamic effect, due to the risen magnetic moment a demagnetization field has
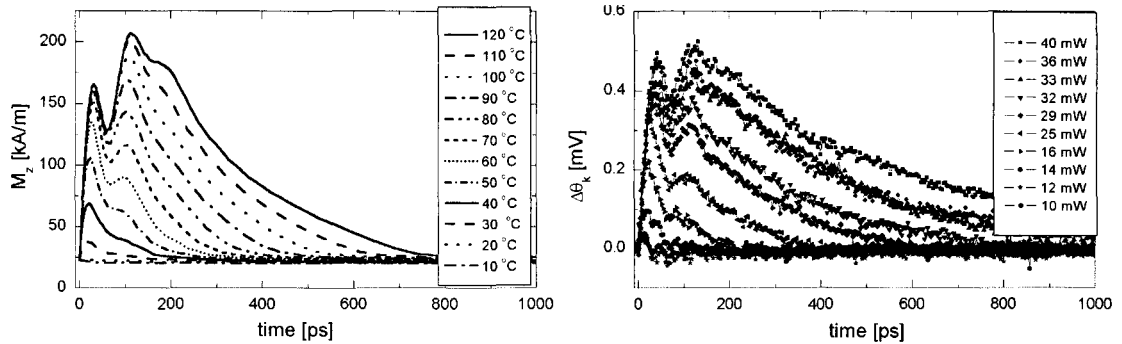
Figure 5.10: Left panel simulation at different temperatures, Used parameters: $\tau_m = 50\text{ps}$, $\tau_s = 0$, $T_0 = 55°\text{C}$, $\delta_{0,Red} = 30\text{nm}$, $\delta_{0,Blue} = 21.2\text{nm}$, $D = 1.994 \cdot 10^{-5}\text{m}^2/\text{s}$, $M_{s,max} = 760\text{kA/m}$, $\alpha = 0.3$, $\gamma_0 = 221 \cdot 10^3\text{m/As}$ and $H_{ext} = 3.5\text{kG}\cdot(e_x, e_z)/\sqrt{2}$.Right panel: measurement at different pump powers, the data also used in [24].

developed and thus the total applied field is changed. According to LLG (equation 3.15) a precession of the magnetization is the response on field changes, causing the second peak.

Depending on the assumptions for the damping term in the LLG, the precession last for the complete time the sample is in the FM phase or is damped already before the second peak set in. In practise a Gilbert damping α of 0.3 turned out to best describe the measurement. This damping is partially intrinsic and partially caused by other effects like decoherence of separate ferromagnetic domains. That there is an non-intrinsic part in the damping obtained in this measurement is proven by other measurements where there exists a third and even a fourth peak.

The measurement in the right panel of figure 5.9 is done with a biconvex lens in the pump beampath with a focal length of 1 meter. This lens causes the pump pulse to diverge and therefore affects the focallength of the objective. Since the objective is not changed the pump pulse will be slightly out of focus while the probe pulse stays in focus as before. With this we tried to prevent for large temperature distributions over the probed sample area. Because the fear is that large temperature distributions can lead to complex convoluted measurement results with areas of quenched magnetization, areas with high magnetization and areas still in the antiferromagnetic phase all together in one signal.

That with this technique indeed the pump spot increased compared to the probe spot is verified by laterally scanning the probe over the sample. Clearly the scanning path with no or only little change in the measured Kerr signal increased with the added lens, although this could not be quantified. Besides a dramatic drop in pump temperature is expected and obtained in the simulations.

To reach larger pump temperatures, also a measurement with a non-diverging pump beam is done. This is presented in figure 5.10, with in the left panel simulations of the probed magnetization and in the right panel the belonging measurements. Clearly there is no large qualitative difference between measurements without temperature distribution over the probed area, figure 5.9, and measurements with some temperature distribution. Further the actual temperature also depends on alignment of other optical components.

In the simulation of this measurement a much larger τ_m is assumed ($\tau_m = 50ps$). To still obtain simulation results in qualitative agreement with the measurement one has to assume a three times larger magnetic moment ($M_{s,max} = 760\text{kA/m}$). Assuming a three times larger magnetic moment than measured with the temperature resolved MOKE measurement can be defended with the fact that later samples with a better annealing procedure obtained
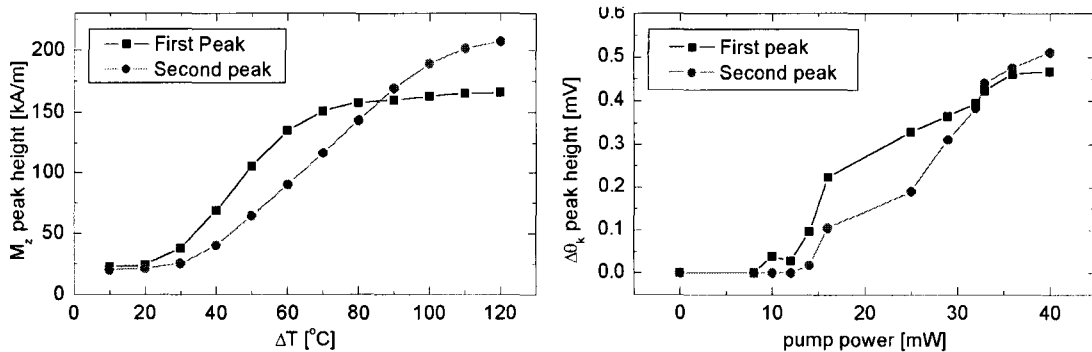
Figure 5.11: Left panel peak height of M_z of first and second peak from the simulation presented in figure 5.10 as function of ΔT. Right panel peakheight of the first and second peak in the measurement of the same figure as function of pump power.

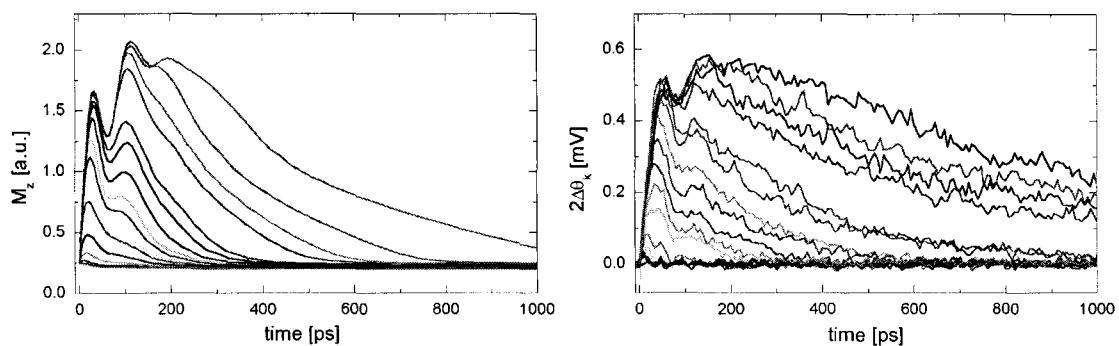
Figure 5.12: Left panel simulation, Used parameters: $\tau_m = 50\text{ps}$, $\tau_s = 0$, $T_0 = 55°\text{C}$, $\Delta T = 11 - 150°\text{C}$, $\delta_{0,Red} = 30\text{nm}$, $\delta_{0,Blue} = 21.2\text{nm}$, $D = 1.994 \cdot 10^{-5}\text{m}^2/\text{s}$, $M_{s,max} = 760\text{kA/m}$, $\alpha = 0.3$, $\gamma_0 = 221 \cdot 10^3\text{m/As}$ and $H_{ext} = 3.5\text{kG}\cdot(e_x, e_z)/\sqrt{2}$. Right panel: Kerr measurement with pump powers between 1.3 and 16.5 mW.

up to a 3.6 times larger magnetic moment. It might be possible that with the small laser spot ($\varnothing \approx 3\mu\text{m}$) different areas of the sample can be selected, this is also supported by the observation of a large signal dependency on sample position. Secondly it might be possible that the laser itself performs a kind of annealing process that increases the magnetic moment.

Though the assumptions for τ_m and $M_{s,max}$ are dependent on one and another, neither of them can be determined exactly with the simulation.

If now the peakheights of the first and second peak of the measurements and the simulations of figure 5.10 are put together, the nice match between measurement and simulation becomes visible, figure 5.11. From this figure one can read that the maximum temperature reached is about 110°C. Indeed larger than in the experiment with lens in the pump beam path.

To be able to do a measurement at higher pump power and with a better signal to noise ratio the setup is realigned. With optimizing all optical components the best possible pump beam parallelism and maximum pump power is obtained. With this new alignment a new measurement is done, presented in figure 5.12. The relative values of the assumed temperatures for the simulations in the left panel of figure 5.12 are equal to the relative pump powers in the measurement. Although much more pump power was available, maximum about 45mW, measurements are not done beyond 16.5mW because higher powers were
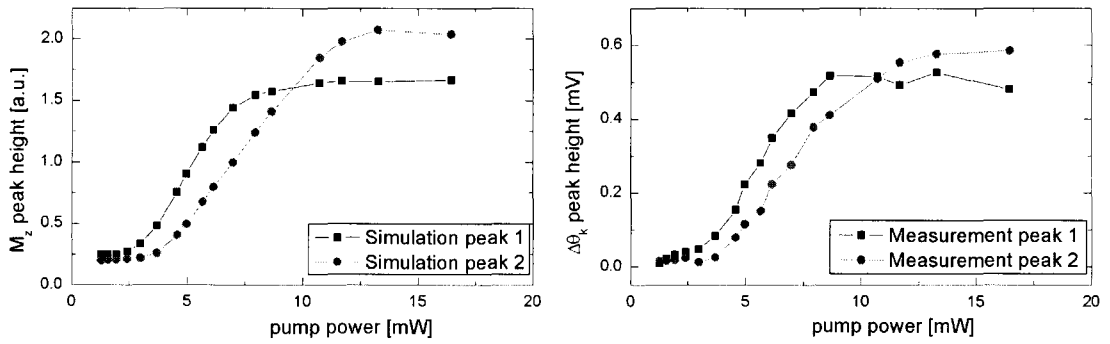
Figure 5.13: Left panel: Peak heights of first and second peak in the simulation as presented in figure 5.12 as function of the matching pump power. Right panel: Peak heights as deduced from measurement presented in the same figure as function of the applied pump power.

destructive before a measurement could be completed. All other parameter assumptions are equal to the simulations in figure 5.10.

This time many features in the measurement are also obtained with the simulation:

- The lowest relative temperature where a small magnetic moment is obtained with the simulation matches the relative power in the measurement.

- At the higher temperatures a first onset of a third peak is visible resulting in a larger ridge after the second peak, in the measurement the third peak is not visible in the noise, but the large ridge is clearly visible.

- The relative temperature where the second peak is just a plateau matches the relative power in the measurement.

- The ratio of peak heights between first and second peak, matches the peak ratio in the measurement at approximately the same relative power.

If now the peak heights of the first and second peak are plotted against the (matching) pump power figure 5.13 is obtained. Clearly visible is the surpass of first peak by the second peak at about 10mW for both the measurement and the simulation. Further also the distance between the first peak and second peak is equal in the simulation and the measurement as well as the height ratio of the peaks.

As noted before, the magnetic moment in the FM-phase also has a contribution to the reflectivity change. Comparison of the normalized reflectivity curves at all different powers makes the magnetic contribution to it visible, figure 5.14. The lowest 4 reflectivity curves are exactly on top of each other (if normalized). This means that there is no magnetic contribution at those low pump-powers because the reached temperatures were below the transition temperature.

At 3.68mW a first escape from the normal reflectivity curve is visible, meaning that the applied pump power was just high enough to change the magnetic phase of the sample. Together with the total maximum temperature as red from figure 5.13 $T_{max} = 205°C$ the background temperature can be solved from the equations:

$$T_0 + \Delta T_{max} = 205°C, \tag{5.10}$$

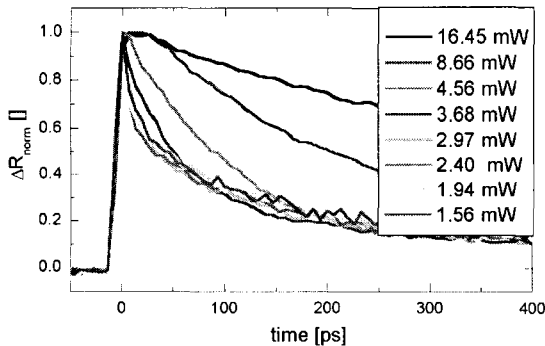$$T_0 + \frac{3.68}{16.45} \Delta T_{max} = T_{trans} = 75°C, \tag{5.11}$$

Figure 5.14: Normalized reflectivity graphs. At the power of 3.68mW and higher clearly a magnetic contribution to the reflectivity is visible. Since maximum power (16.45mW) equals to a total temperature of 205°C (as will be deduced from figure 5.15) the base temperature is $T_0 = 33°C$ and $\Delta T_{max} = 167°C$.

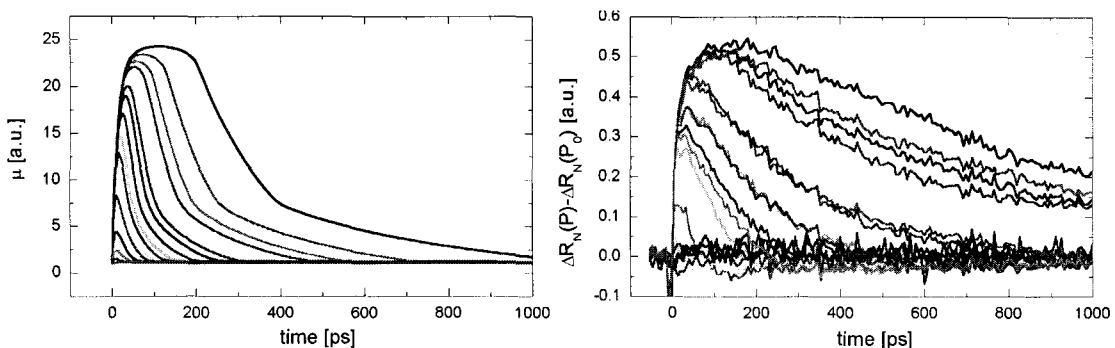Figure 5.15: Left panel: Simulation of magnetic moment, i.e. the simulation without the LLG dynamics, Used parameters: $\tau_m = 10ps$, $\tau_s = 0$, $T_0 = 55°C$, $\Delta T = 11 - 150°C$, $\delta_{0,Red} = 30nm$, $\delta_{0,Blue} = 21.2nm$, $D = 1.994 \cdot 10^{-5}m^2/s$, $M_{s,max} = 250$ kA/m. Right panel: Difference of normalized reflectivity graphs at different powers and the normalized reflectivity at the lowest power (temperature stays below the transition temperature).

and thus $\Delta T_{max} \approx 167°C$ and $T_0 \approx 37°C$.

If now the lowest-power reflectivity curve is subtracted from the higher power curves, a curve representing the build up and run down of magnetic moment is obtained, see figure 5.15. These curves represent the magnitude of magnetization independent on the direction of magnetization. Simulations can thus be made with the same assumptions as before but without the angular dynamics of the LLG equation.

The low-power curves in figure 5.15 do not reach maximum magnetization before the sample cools down through the transition temperature back to the AFM-phase. At high pump power (top three reflectivity curves) the sample stays long enough in the FM-phase to completely build up the maximum magnetic moment. Then, while the sample cools towards the transition temperature, the magnetic moment increases further towards maximum magnetization at the transition temperature. Therefore the time to reach the maximum in the highest three curves is much longer than the times in the other curves.

To further establish the precessional origin of the double peak behavior a field dependent measurement is done. The right panel of figure 5.16 displays some typical Kerr measurements. It turned out that at higher fields the magnetization is higher and the damping is lower. This can be explained qualitatively. At high fields, alignment of separate magnetic
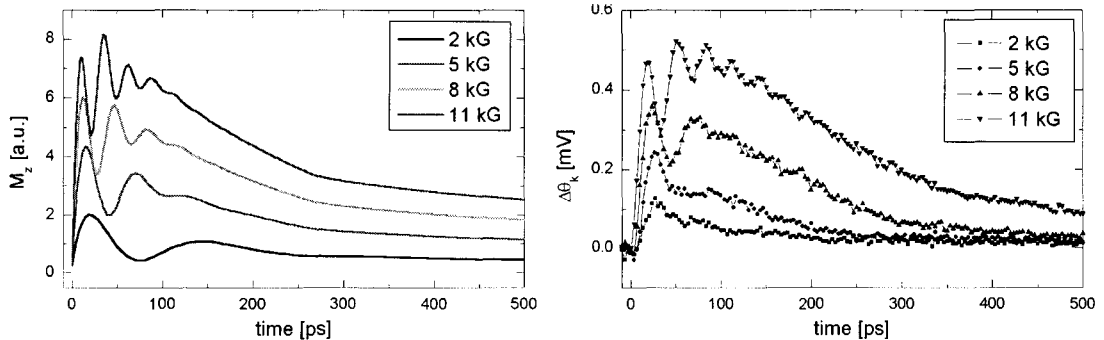
Figure 5.16: Left panel: Simulation, Used parameters: $\tau_m = 10\text{ps}$, $\tau_s = 0$, $T_0 = 65°\text{C}$, $\Delta T = 75°\text{C}$, $\delta_{0,Red} = 30\text{nm}$, $\delta_{0,Blue} = 21.2\text{nm}$, $D = 1.994 \cdot 10^{-5}\text{m}^2/\text{s}$, $M_{s,max} = 760\text{kA/m}$, $\alpha = 0.3, 0.25, 0.2, 0.15$ respectively, $\gamma_0 = 221 \cdot 10^3\text{m/As}$ and $H_{ext} = 2, 5, 8, 11kG$ respectively. Right panel: Measurement at 2,5,8,11 kG respectively.

domains is more effectively and a spreading in crystalline anisotropy and spreading in shape anisotropy is neutralized, resulting in higher magnetic moments and thus an higher Kerr signal. Also due to the same effect spreading in magnetic moment directions is lower at high fields causing less decoherence in the precessional motion, i.e. less apparent damping.

5.4 Conclusions and Recommendations

The metamagnetic phase change in FeRh takes place in approximately 30ps when heated with an ultrafast optical pulse. The magnetization dynamics, once in the ferromagnetic phase, are well described by a simple model using LLG and four principal assumptions:

1. Initial growth of first magnetization moments is in the direction of the external field

2. Heat diffusion only takes place in the perpendicular direction.

3. Exchange interaction is infinitely strong throughout the sample thickness.

4. The demagnetizing field is equal but opposite to the magnetization in the z-direction averaged over the sample thickness.

With a simulation based on only those four assumptions the Kerr measurements on FeRh were obtained with high qualitative resemblance and even some quantitative similarities. Therefore growing ferromagnetic moment in the direction of applied field and precession thereafter is a very likely model describing the ultrafast phase change from antiferromagnetic to ferromagnetic in FeRh. Further the possibility of a depth effect causing a double peak behavior is not very likely due to the extreme assumptions necessary to obtain a qualitative match with the measurements and due to a definite absence of third and fourth peaks as observed in several measurements. Finally also a delayed temperature model is not very likely because if that would be the cause then the first peak would extend with increasing pump power, contrary to the measurements.

For further analysis of magnetic phase changes in FeRh it would be good to have a thinner and more flat sample with less lateral anisotropy changes. With such a sample more intrinsic Gilbert damping and field dependencies can be obtained. The relatively high magnetic moment assumed in the simulations can than be checked.

Furthermore it would be interesting to change the field angle and also measure the magnetization with inplane field and the longitudinal Kerr effect, the precessional behavior should vanish if the field is appropriate aligned in the sample plane.

The temperature obtained with a pump pulse can be further checked when a bias sample temperature is applied with an continuous heating stage. Although the remark here has to be made that heating with a heating stage is different in several ways than heating with a pump pulse. With a pump pulse, for example, heating is very localized to a small spot and a short timeframe. The lattice barely gets enough time to expand in the perpendicular direction and does not get enough space to expand in the lateral directions. Therefore the phase transition in FeRh driven by temperature might be at a different temperature and different time scale than phase transitions in FeRh driven by optical pump pulses.

Measurement of the phase transition with a very large time resolution would be very interesting. With careful measurements during the first 30ps more information about the physical process of magnetic phase transitions might be revealed.

6 Conclusions

A pump probe setup has been developed and improved to measure precession dynamics in perpendicular recording media (PMR) as well as phase change dynamics in FeRh thin film.

Precession measurements on PMR media with different grain exchange coupling have been performed and Gilbert damping constants are deduced from the precession dynamics. Although comparison of measured precessions in one dimension with simulated LLG precessions is difficult, it resulted in some strong dependencies of the Gilbert damping parameter α on several quantities. The dependencies are so strong that eventual errors produced by the method can not fully explain the tremendous changes in the Gilbert damping. The Gilbert damping parameter α is measured as a function of applied field, pump power and grain exchange decoupling. Especially the pump power dependence of the damping in PMR media is tremendous.

More measurements with changing field angle, changing sample bias temperature and measurements on simple homogeneous films of ordinary elements must reveal the origin of the strong dependencies of α.

Pump-probe measurements on FeRh thin film gave the for the first time experimental evidence of an ultrafast magnetic phase change from antiferromagnetic to ferromagnetic. Recorded times are in the order of 20-30 picosecond when driven by a 100 femtosecond optical pump pulse. Further analysis of the obtained transient Kerr and reflectivity curves resulted in a proposed model describing the observed effects very well in a qualitative way.

More measurements with high temporal resolution might reveal more of the physical process originating on the magnetic phasechange. Measurements dependent on the angle of the applied field can be done for further analysis of the magnetization dynamics after the phase change took place. Pump-probe measurements with a bias temperature are an interesting option for the analysis of the temperature dependence of the magnetic phase change.

Bibliography

[1] E. Grocowski. Ibm almaden research laboratories. www.storage.ibm.com.

[2] R.L. Comstock. Review modern magnetic materials in data storage. *Journal of Materials Science in Electronics*, 13:509–523, 2002.

[3] T.C. Arnoldussen. Bit cell aspect ratio: An snr and detection perspective. *IEEE Transactions on Magnetics*, 34(4):1851–3, July 1998.

[4] D. Weller. Thermal effect limits in ultrahigh-density magnetic recording. *IEEE Transactions on Magnetics*, 35(6):4423–39, 1999.

[5] E.N. Abarra. Longitudinal magnetic recording media with thermal stabilization layers. *Applied Physics Letters*, 77(16):2581–3, October 2000.

[6] E.E. Fullerton. Antiferromagnetically coupled magnetic media layers for thermally stable high-density recording. *Applied Physics Letters*, 77(23):3806–8, December 2000.

[7] M.H.Kryder. Future trends in magnetic storage technology. In IEEE, editor, *DIGEST Joint PMRC 2003. 2nd North American Perpendicular Magnetic Recording Conference*, 2003.

[8] Jan-Ulrich Thiele. Ferh/fept exchange spring films for thermally assisted magnetic recording media. *Applied Physics Letters*, 82(17):4, April 2003.

[9] J. Hohlfeld. *Ultrafast Electron-, Lattice-, and Spin-Dynamics in Metals Investigated by Linear and Nonlinear Optical Techniques*. Ph.d. thesis, Freien Universitt Berlin, 1998.

[10] E. Beaurepaire. Ultrafast spin dynamics in ferromagnetic nickel. *Physical Review Letters*, 76(22):4250, May 1996.

[11] X.W. Wu. Magnetic anisotropy and thermal stability study on fept nanoparticle assembly. *Aplied Physics Letters*, 82(20):3475–7, May 2003.

[12] M. van Kampen. All-optical probe of coherent spin waves. *Physical Review Letters*, 88(22):227201, June 2002.

[13] K. Ounadjela B. Hillebrands, editor. *Spin Dynamics in Confined Magnetic Structures II*, volume 87 of *Topics in Applied Physics*, chapter B. Koopmans, Laser-Induced Magnetization Dynamics, pages 253–320. Springer-Verlag, 2003.

[14] J.T. Wolfson. Front-end write process model for high data rate longitudinal magnetic recording. *IEEE Transactions on Magnetics*, 40(1):275–280, Januari 2004.

[15] V.L. Safonov. Nonlinear microscopic relaxation of uniform magnetization precession. *Journal of Applied Physics*, 93(10):6912–6914, May 2003.

[16] Y.Tserkovnyak. Enhanced gilbert damping in thin ferromagnetic films. *Physical Review Letters*, 88(11):117601 1–4, March 2002.

[17] A.W. Spargo. Gilbert damping in polycrystalline thin films. *Journal of Magnetism and magnetic materials*, 2003(258-259):35–38, 2003.

[18] J. Wu. Excitation and damping of spin excitations in ferromagnetic thin films. *Journal of Magnetism and magnetic materials*, 241:96–109, 2002.

[19] J.H.H. Rietjens. Precessional magnetization dynamics in micron sized ferromagnetic elements. Master thesis, Eindhoven University of Technology, Den Dolech 1, 5612 MB, Eindhoven, April 2004.

[20] Qiang Zhang. Coherent magnetization rotation and phase control by ultrashort optical pulses in cro_2 thin films. *Physical Review Letters*, 89(17):177402–1–4, October 2002.

[21] W. Platow. Correlations between ferromagnetic-resonance linewidths and sample quality in the study of metalic ultrathin films. *Physical Review B*, 58(9):5611, September 1998.

[22] M.E. Gruner. Instability of the rhodium magnetic moment as the origin of the metamagnetic phase transition in ferh. *Physical Review B*, 67(64415):10, 2003.

[23] C. Kittel. Model of exchange inversion magnetization. *Physical Review*, 120(2):335, October 1960.

[24] G. Ju. Ultrafast generation of ferromagnetism via antiferromagnet to ferromagnet transformation in ferh thin film. *In preparation*, 2004.

7 Acknowledge

With the preparation of this internship at Seagate as well as the internship itself I luckily obtained lots of cooperation. First of all I need to thank Bert Koopmans, for bringing me in contact with Seagate, for the help during the project but especially for the extended and detailed comments during the writing of this thesis.

With Ganping Ju it was nice to work, many fruitful discussions leaded to new ideas, new samples and new equipment. With his enthusiasm he often motivated me (to do another measurement). Ganping thanks for the beers at Valhalla's. Thanks to Julius Hohlfeld there was always somebody in the lab, giving a never ending source of very fruitful "just one crazy idea"-s. Rene van de Veerdonk also often had good ideas for improvement of measurement and setup. Moreover he often participated when it came to programming tasks or questions about it.

I am very grateful to Seagate for receiving me as a winter-"summer-intern" at their top of the bill research facility and giving me the opportunity to have a look behind the scenes of a hardrive manufacturer. With Nils Gokemeijer I saw my freetime occupied with rowing workouts. Thanks to Nils we had a wonderful Seagate team and we have beaten the Heinz team at the Keystone regatta.

With Roy from PYP I had a good friend outside Seagate to show me the real life in the USA and with Chritophe and Dorothea I had some good friends to discuss typical American habits. Thank you all for the great time I had during my internship in the USA.

Bastiaan Bergman.